

EXOPLINES: Molecular Absorption Cross-Section Database for Brown Dwarf and Giant Exoplanet Atmospheres

EHSAN GHARIB-NEZHAD,^{1,2,3,*} AISHWARYA R. IYER,⁴ MICHAEL R. LINE,⁴ RICHARD S. FREEDMAN,^{5,1} MARK S. MARLEY,¹
AND NATASHA E. BATALHA¹

¹NASA Ames Research Center, Moffett Field, CA 94035, USA

²Bay Area Environmental Research Institute, NASA Ames Research Center, Moffett Field, CA 94035, USA

³School of Molecular Sciences, Arizona State University, Tempe, AZ 85281, USA

⁴School of Earth and Space Exploration Arizona State University, Tempe AZ 85281, USA

⁵SETI Institute, Mountain View, CA 94035, USA

ABSTRACT

Stellar, substellar, and planetary atmosphere models are all highly sensitive to the input opacities. Generational differences between various state-of-the-art stellar/planetary models are primarily because of incomplete and outdated atomic/molecular line-lists. Here we present a database of pre-computed absorption cross-sections for all isotopologues of key atmospheric molecules relevant to late-type stellar, brown dwarf, and planetary atmospheres: MgH, AlH, CaH, TiH, CrH, FeH, SiO, TiO, VO, and H₂O. The pressure and temperature ranges of the computed opacities are between 10⁻⁶–3000 bar and 75–4000 K, and their spectral ranges are 0.25–330 μm for many cases where possible. For cases with no pressure-broadening data, we use collision theory to bridge the gap. We also probe the effect of absorption cross-sections calculated from different line lists in the context of Ultra-Hot Jupiter and M-dwarf atmospheres. Using 1-D self-consistent radiative-convective thermochemical equilibrium models, we report significant variations in the theoretical spectra and thermal profiles of substellar atmospheres. With a 2000 K representative Ultra-Hot Jupiter, we report variations of up to 320 and 80 ppm in transmission and thermal emission spectra, respectively. For a 3000 K M-dwarf, we find differences of up to 125% in the spectra. We find that the most significant differences arise due to the choice of TiO line-lists, primarily below 1 μm. In sum, we present (1) a database of pre-computed molecular absorption cross-sections, and (2) quantify biases that arise when characterizing substellar/exoplanet atmospheres due to line list differences, therefore highlighting the importance of correct and complete opacities for eventual applications to high precision spectroscopy and photometry.

Keywords: Brown dwarfs (185), Exoplanet atmospheres (487), Exoplanet atmospheric composition (2021)

1. INTRODUCTION

Over the past two decades, atmospheric characterization of exoplanets and brown dwarfs has been dramatically increasing—particularly, observations with *HST*, *Spitzer*, various ground-based telescopes both with low to moderate resolution spectroscopy and high-resolution cross-correlation approaches (e.g., Madhusudhan 2019). Additionally, with the Transiting Exoplanet Survey Satellite (*TESS*), in conjunction with the launch of

the James Webb Space Telescope (*JWST*), we can expect hundreds of planet detections (Sullivan et al. 2015; Louie et al. 2018; Kempton et al. 2018) followed by detailed spectroscopic characterization of their atmospheres (Greene et al. 2016; Bean et al. 2018). The compositional and temperature diversity of these worlds provide a unique opportunity to gain insight into planetary atmospheric chemical processes and formation pathways (Öberg et al. 2011; Fortney et al. 2013; Mordasini et al. 2016; Hörst et al. 2018).

Fully capitalizing on the information encoded in a spectrum, therefore, requires a robust model interpretation. Models used to interpret thermal emission spectra (either from an isolated object like a brown dwarf, M-

Corresponding author: Ehsan Gharib-Nezhad
e.gharibnezhad@asu.edu

* NASA Postdoctoral Fellow

dwarf, or directly imaged planet, or a secondary eclipse spectrum for a transiting planet) and transmission spectra (for transiting planets) require some combination of chemistry and radiative transfer. Self-consistent models (either 1D or 3D) rely upon a detailed coupling between chemical processes (e.g., thermochemical equilibrium or chemical kinetics/photochemistry), radiative energy transport, convective/dynamical energy transport, and cloud/haze processes to determine the atmospheric state and subsequent observables (e.g., [Marley & Robinson 2015](#); [Zhang 2020](#), and references therein). Retrieval models, on the other hand, are purely data-driven and attempt to leverage large numbers of free parameters (e.g., molecular abundances for selected species, temperature profile parameterization) to adequately fit the observables to determine Bayesian constraints on composition, clouds, and thermal structures ([Line et al. 2014](#)). The adequacy of these methods, whether for predictions or parameter estimation, relies upon accurate and complete molecular and atomic opacities.

In this work, we focus on high-resolution (adaptive R, e.g., 2×10^4 – 2×10^6 at $1 \mu\text{m}$) opacities with implications to Ultra-Hot Jupiter atmospheres. Our prime candidates being TiO, VO, MgH, AlH, CaH, TiH, CrH, FeH, and SiO—the key molecules¹ in such atmospheres. In addition, we generate H₂O high-resolution opacities from 500–4000 K, which is required for modeling everything from super-Earth to M-dwarf atmospheres. Starting with §2, we first provide an astrophysical context for the importance of metal hydrides and oxides in substellar atmospheres. §3 provides discussion on the current state of opacity or absorption cross-section data, highlighting line broadening effects that are missing and how we tackle them. In §4, we bridge the gap by providing pre-generated absorption cross-sections for the metal hydrides and oxides in question, alongside comparisons with previous efforts. In §5, we quantify the effect of opacity differences on transmission and emission spectra of a representative² Ultra Hot Jupiter planet, followed by M-dwarf stellar spectra in §6, and potential biases and challenges with opacities that arise in atmospheric characterization efforts, described in §7. Finally, we present a brief summary of our conclusions in §8. The main outcome of this work is EXOPLINES absorption cross-section database (i.e., EXOplanet Pressure-broadened LINES).

¹ For further study on the composition of these ultra-hot Jupiters and M-dwarfs, studies by [Lodders & Fegley \(2006\)](#) and [Visscher et al. \(2010\)](#) are suggested.

² “representative” in this context means a generic atmospheric case

2. ASTROPHYSICAL IMPORTANCE

Temperature and pressure play a key role in controlling molecular and atomic abundances that ultimately shape a spectrum (e.g., [Burrows & Sharp 1999](#)). At cooler temperatures (< 200 K), solar system giants are dominated by absorption because of methane and scattering by clouds, and photochemically produced hydrocarbons. At warmer temperatures (300–1000 K), T-dwarfs, and many (sub)Neptune transiting planet atmospheres are sculpted (or presumed to be sculpted) by water, methane, ammonia, and alkali metals. Higher temperature results in the onset of CO absorption, followed by several oxides (TiO, VO) and hydrides (FeH, CrH, MgH, CaH), especially above 1500 K. The increasing presence of these species as a function of temperature is what ultimately (along with dust/condensate formation) governs the M-L-T-Y dwarf classification sequence and their sub-types ([Kirkpatrick 2005](#)). Furthermore, water dissociation, the onset of H-bound/free-free, and contribution of refractory atoms and their ions (e.g., Fe, Ti, Mg, Ca, Si) dominate atmospheres with temperatures above ~ 2500 K, encountered in M-dwarfs and ultra-hot Jupiters ([Lodders 1999](#)). Here, we highlight the importance of these metal oxides and hydrides and their behavior in high-temperature regimes—particularly in substellar atmospheres of M/L-type Dwarfs and highly irradiated exoplanets.

2.1. Metal Oxides

M-dwarf stars ($2000 \text{ K} < T_{\text{eff}} < 4000 \text{ K}$), active photospheric spots on sun-like stars, and even highly irradiated exoplanets with similar effective temperatures have atmospheres that are all dominated by TiO ([Kirkpatrick et al. 1991](#); [Webber 1971](#)). Covering the optical spectral region between 630–900 nm, TiO plays a vital role in the proper characterization of M-dwarfs and Ultra-Hot Jupiters. The temperature dependence of TiO governs the energy level populations that affect the relative band-structure intensities, an essential tool in classifying early-type M-dwarfs ([Sharpless 1956](#)). For instance, in spectra of M0–M3 dwarfs, the 0–0 band³ (705.4 nm) is used as the primary classification marker. The strongest TiO bands near 843 nm, 819.4 nm to 885.9 nm, and 660 to 710 nm are important indicators for M4, M6, and late-type M8 dwarfs respectively ([Sharpless 1956](#); [Lockwood 1972](#); [Ruiz et al. 1997](#); [Delfosse et al. 1997](#)).

Similar to TiO, VO is a refractory molecule in M-dwarfs and early L-dwarf atmospheres ($\sim L2$). With

³ In spectroscopy, the $\nu' - \nu''$ band refers to all rotation-vibrational transitions between the upper vibrational level, ν' , and the lower vibration level ν'' ([Bernath 2005](#)).

strong spectral signatures between 0.6–1.5 μm , metal oxides such as VO are sensitive temperature indicators in substellar atmospheres (Cushing et al. 2005). The strength of the VO absorption features at 1.17 and 1.22 μm , combined with TiO and CaH bands, are valuable spectroscopic youth indicators for brown dwarfs (Kirkpatrick et al. 2006; Peterson et al. 2008).

In addition to their importance for substellar spectral and age classification, high-temperature oxides are critical sources of opacity in the optical wavelength region, that drive heating in the upper atmospheres of hot Jupiters (>1800 K and <50 mbar)—essential for proper characterization of the 1D vertical structure of the atmosphere (Hubeny et al. 2003; Fortney et al. 2008). The presence of TiO and VO drive up stellar irradiation mean opacity relative to the planetary thermal emission mean opacity, resulting in a “thermal inversion” (increasing temperature with decreasing pressure) in the planetary atmosphere. However, we note that bonafide detection of metal oxides (TiO or VO) has remained elusive and somewhat controversial, partially due to the inadequacy of the opacity data for these species (Merritt et al. 2020; Nugroho et al. 2017).

In substellar atmospheres, especially at temperatures cooler than 2300 K, both TiO and VO gradually disappear due to condensate formation (TiO into CaTiO₃ and VO turns into solid VO, Lodders (1999)). Therefore, their spectral features are not prominent at such atmospheres at $\sim 0.7\text{--}1.2$ μm , allowing for metal hydride FeH, CrH, and CaH features to present themselves.

2.2. Metal Hydrides

Several FeH features within the 0.7–1.3 μm range has been detected in the late-M and L dwarfs (Kirkpatrick et al. 2000), including the 0–0 band (known as the Wing-Ford band) at 0.985–1.02 μm (Cushing et al. 2003), the 1–0 band at 869.2 nm in L-dwarfs (Kirkpatrick et al. 1999), the 2–0 band at 778.6 nm, the 1–0 band at 869.2 nm, the 2–1 band at 902.0 nm (Tinney & Reid 1998) and the 1–2 band at 1238.9 nm bands are present in very low-mass stars (Reid et al. 2001). Additionally, Schiavon et al. (1997) showed that the Wing-Ford band is sensitive to surface gravity and metallicity. Similar to FeH, CaH, CrH, and AlH all show a strong dependence on surface gravity (see Chapter 4 in Reid & Hawley (2005)).

The CrH 0–0 (861.1 nm) and 0–1 (996.9 nm) bands along with the FeH bands (and their ratios) serve as diagnostic indicators (Kirkpatrick et al. 1999, 2000) for classifying the L-dwarf sub-types (see Table 6 in Kirkpatrick et al. (1999)).

In the context of Ultra-Hot Jupiters, species like MgH, AlO, NaH, and CaO could also drive thermal inversions depending on elemental abundance ratios (Gandhi & Madhusudhan 2019). Additionally, hydrides such as MgH, CrH, CaH, and FeH although expected to be present in hot Jupiter atmospheres; the lack of reliable detections have made it difficult to assess their true role in governing the 1-D thermal structure.

3. METHODOLOGY: MOLECULAR ABSORPTION CROSS-SECTIONS

The absorption cross section⁴ (hereafter ACS) of an absorber is governed by the wavelength-dependent intensity, position, and width of a spectral line. The line shape is typically modeled with a Voigt profile, which is a convolution of Doppler (thermal) and pressure (Lorentz or collisional) broadening. Uncertainties in the line positions, strengths, and widths are ultimately what drive the uncertainties or inadequacies in various pre-computed ACSs. Below we present the formulation of line profile in §3.1, and then we extend our discussion on pressure-broadening and their availability in §3.2, followed by the treatment for their J -dependency and wing cut-off in §3.3–3.4. Finally, §3.5 describes the line-list data structure, and computational details are provided in §3.6.

3.1. Line-width

The conventional form of the spectral line shape is the Voigt profile, which is a convolution of Doppler and Lorentz profiles. Doppler broadening is governed by the temperature, molecular mass, and also the transition energy, and its half-width at half-maximum width (HWHM), Γ_D , may be given by (Buldyreva et al. 2011):

$$\Gamma_D = 3.581 \times 10^{-7} \sqrt{\frac{T}{M}} \nu \quad (1)$$

where M is absorbers molecular mass in amu (atomic mass unit), T is the temperature (in K), and ν is the line position in wavenumber (cm^{-1}).

Lorentz line profile is controlled by the magnitude of the interaction between the absorber and broadening gas species, and the Lorentz HWHM, Γ_L , depends on

⁴ Both opacities and absorption cross-sections represent the capability of species (i.e., atom, molecule, or radical) to absorb or emit light. However, their definitions are different. Opacity κ is the “effective area” of one gram of an absorber (unit: cm^2/gram) to absorb/emit light while absorption cross-section σ is the “effective area” of one absorber (unit: $\text{cm}^2/\text{molecule}$). These quantities are interchangeable with $\kappa\rho = \sigma n$ equation, where ρ is mass density (gram/cm^3) and n is number density ($\text{molecule}/\text{cm}^3$).

the temperature and the broadening species and can be described by

$$\Gamma_L = \sum_b \left(\frac{T}{296\text{K}} \right)^{-n_{T,b}} \gamma_{L,b} p_b \quad (2)$$

where $\gamma_{L,b}$ is the Lorentz coefficient of an absorber (HWHM, unit: $\text{cm}^{-1}/\text{bar}$), p_b is the broadener partial pressure (unit: bar), and $n_{T,b}$ is the temperature-dependence coefficient, which is dimensionless. Both $\gamma_{L,b}$ and $n_{T,b}$ are controlled by broadener-absorber interaction and the quantum properties of absorbing molecules.

Quantifying $\gamma_{L,b}$ and $n_{T,b}$ coefficients for the metal hydrides/oxides in question (e.g., TiO, VO, MgH, etc.) are challenging aspects of ACS calculations because there is not any laboratory or computational measurements have been done to determine their $\gamma_{L,b}$ and $n_{T,b}$ coefficients⁵.

3.2. Estimating the Lorentz Coefficient

Theoretically determining the Lorentz coefficient is quite challenging because it depends on molecular quantum properties such as total rotational angular momentum⁶, molecular symmetries, and environmental conditions like temperature and the background gas broadener composition. For TiO, VO, TiH, CrH, the Lorentz coefficients have been estimated up to low J quantum numbers (given in Table 1) for H_2/He atmospheres. These estimations are based on the similarity between the molecular symmetry or dipole moments that these absorbers have with the available Lorentz coefficients (e.g., Freedman et al. 2014; Chubb et al. 2020)⁷. In reality, we do not have enough or even a single measurement for the metal hydrides/oxides in this study (except H_2O) at any temperature (see §7 for the challenges we are dealing with these opacities).

Due to the lack of $\gamma_{L,b}$ and $n_{T,b}$ coefficients, we used the classical collision theory by Anderson (1949) in order

to estimate the Lorentz coefficient using the following equation (see §A.1 for further discussion):

$$\gamma_{L,b} = 0.0567 (T\mu)^{-1/2} \sigma_{\text{col},b} \quad (3)$$

where μ is the reduced mass of the absorber-broadener pair in amu, $\sigma_{\text{col},b}$ is the collision cross-section in \AA^2 of the broadener b , and $\gamma_{L,b}$ is in $\text{cm}^{-1}/\text{atm}$. In this equation, the collision (or scattering) cross section, $\sigma_{\text{col},b}$ is a fundamental factor, that connects collisions in the microscopic world into the spectral linewidth. For further details, see studies by Odashima et al. (1989) and Gierszal et al. (1998) that have used this approach to calculate the collision cross section from the laboratory-measured Lorentz line width. In addition, Cappelletti et al. (2005) have shown a good agreement between the experimental and computed pressure-broadening coefficients of $\text{C}_2\text{H}_2\text{-Ar}$ system.

Even though Eq. 3 is derived from the collision theory, it has some limitations and errors such as ideal gas assumption and also possible inaccuracy in the computed collision cross-section data from ab-initio methods. Hence, this equation and the calculated pressure-broadening coefficients will not fulfill the lack of laboratory measurements or theoretical calculations. For example, the modified semi-classical Robert Bonamy theory (Robert & Bonamy 1979; Ma et al. 2007) have been successfully implemented to calculate the half-width and line shift of H_2O and CO absorbers in different broadening gases (e.g., Gamache & Vispoel 2018; Vispoel et al. 2020), and so similar studies are required for these molecules in question.

Note that the assumption of 0.5 for the temperature-dependence coefficient, $n_{T,b}$ at Eq. 3 is based on the kinetic theory, while laboratory measurements of other species suggest $n_{T,b}$ can vary from 0.2–1.2. In turn, $n_{T,b}$ can strongly depend on the broadener and J quantum number (e.g., CH_4 in different broadening gas that have shown in table 5 by Gharib-Nezhad et al. (2019)), or $n_{T,b}$ may be roughly constant with J (e.g., CO-self/air broadening by Devi et al. (2012)). Wagner et al. (2005) have measured the effect of H_2O -air mixture and found that $n_{T,b}$ can also be negative number. Table 2 represents the collected collision cross sections, σ_{col} for CaH and SiO absorbers for H_2 or He broadeners where available for $J_{\text{lower}}=0$. In addition, the AlH $\gamma_{L,b}$ coefficient is assumed to be equal to the CO broadening coefficient because of their similar dipole moments (we adopt this approach from Freedman et al. (2014) and Chubb et al. (2020) approaches.)

⁵ More precisely, we could find only one spectroscopic measurement of AlH in H_2 gas by Watson & Hull (1936). Their measured γ_L is $0.24 \text{ cm}^{-1}/\text{atm}$, which looks much larger than the available H_2 -broadening data for other well-known absorbers. Given the limitation in pressure gauges, spectrometers, and thermometers in their measurements in the 1930s, we decided not to use their number.

⁶ In fact, each transition has its corresponding rotational and vibrational quantum numbers and molecular symmetries, which are controlling the Lorentz coefficient and hence the spectral linewidth.

⁷ For instance, Chubb et al. (2020) used HCN broadening coefficients for computing the ACS data of CaH, CrH, SiO, TiO, and VO absorbers, as well as HF broadening coefficients data for FeH and TiH.

3.3. Estimating the Behavior of Pressure-Broadening Coefficients and Their Dependence on J Quantum Numbers

The calculated or estimated Lorentz coefficients, $\gamma_L(J)$ depend on J quantum numbers. To understand the behavior of $\gamma_L(J)$ for all J s, we need to consider two issues: 1) the degree or rate of the $\gamma_L(J)$ decrease with J (or $\frac{\partial \gamma}{\partial J}$), and 2) an equation that can extrapolate these J -dependence behavior without becoming negative or increasing sharply.

The first issue can be tackled by comparing the J -dependence behavior of the available $\gamma_L(J)$ coefficients of diatomic molecules with H_2 and He broadening. For example, the Lorentz coefficient of CO molecule (with low dipole moment) has a smooth decrease with high J s (Devi et al. 2004; Régalia-Jarlot et al. 2005; Mantz et al. 2005). In contrast, for absorbers with large dipole moments such as HCl- H_2 and HCl-He systems, $\gamma_L(J)$ value drop noticeably according to the laboratory measurements done by Toth et al. (1970), Li et al. (2018), Babrov et al. (1960) (see Fig. 1). All the metal hydrides and oxides in question (except AlH) have large dipole moments, and for the lack of any other information we assume that their J -dependency may decrease similar to HCl. However, one should keep in mind that dipole moment values are not major factors in the rotational dependence of the broadening parameters. Detailed discussion on the reason for J -dependence of spectral lines is provided by Hartmann et al. (2021) (chapter 3) and Renaud et al. (2018). The second issue may be solved by using the proposed equation by the HITRAN group⁸ (e.g., see Gordon et al. 2017, and their upcoming paper, Gordon et al. 2021). As part of their group efforts, Tan et al. (2019) have examined the fitting accuracy of the available pressure-broadening coefficients for water as a broadener and several terrestrial key absorbers (e.g., CO, CO₂, CH₄); and they suggested the fourth-order Padé approximant as the most reliable prediction of the Lorentz J -dependency. Fourth-order Padé equation provides a smooth decrease of γ_L with J and has the following form:

$$\gamma_L(J) = \frac{a_0 + a_1J + a_2J^2 + a_3J^3}{1 + b_1J + b_2J^2 + b_3J^3 + b_4J^4} \quad (4)$$

where a_0 to a_3 and b_1 to b_4 are the fitting coefficients. J is also the lower total angular quantum number. Besides, we applied the following constraints to this equation to avoid negative numbers of γ_L as well as follow

a sharp J -dependency for absorbers with large dipole moments (i.e., MgH, CaH, CrH, FeH, TiH):

$$\begin{aligned} \gamma_L(J = 10) &= \sim 0.5\gamma_L(J = 0) \\ \gamma_L(J = 40) &= \sim 0.1\gamma_L(J = 0) \\ \text{if } \gamma_L(J > 40) < 0 & \Rightarrow \gamma_L(J) = \gamma_L^{\min} - \left(\frac{1}{J} * \gamma_L^{\min}\right) \end{aligned} \quad (5)$$

An example of the calculated broadening coefficients for the metal hydrides/oxides in question is presented in Fig. 2. Additionally, the Fourth-order Padé coefficients for all the absorbers in this study are listed in Table 3 and are valid up to $J=500$.

3.4. Wing cut-off

Wing cut-off is an important challenge in fully and accurately computing the opacity continuum (see §7). Given the lack of sufficient pressure broadening data for these species and the huge computational time, the Voigt profile is implemented in various pre-computed opacity data. The current method to deal with this non-Lorentzian behavior of the Voigt profile is either using absolute wavenumber such as 100 cm^{-1} (e.g., MacDonald 2019) or just using multiplication of the Voigt profile (e.g., 200 to 500 of Voigt HWHM) (e.g., Chubb et al. 2020; Freedman et al. 2014).

Note that several laboratory and theoretical studies have shown that non-Voigt behavior provides a more accurate opacity continuum (e.g., Ngo et al. 2012). For example, Hartmann et al. (2002) have recorded the 3.3 μm spectrum of CH₄ in H_2 bath gas and have shown that the Voigt behavior is valid up to 25 cm^{-1} from the line center. Inspiring by their results, we decide to use absolute number for the wing cut-off as follow: 30 cm^{-1} for $P \leq 200$ bar and 150 cm^{-1} for $P > 200$ bar. We noticed that Mollière et al. (2019) have considered this method as well in calculating their opacities.

It is worth mentioning that we did not use the multiplication factor of the Voigt linewidth because for a generic spectral line at low-to-moderate pressure and at the infrared spectral region with small wavenumber (such as $P < 10^{-3}$ bar at $< 1000 \text{ cm}^{-1}$), the 500 \times Voigt-half-width will be less than 10 cm^{-1} which is not sufficiently high value for the wing cut-off according to the results by Hartmann et al. (2002). Additionally, for high pressures (such as $P > 100$ bar), this 500 \times Voigt-HWHM is a large number even larger than 500 cm^{-1} which results in an extreme overestimation.

3.5. Line List

A typical line-list data contains all of the necessary ingredients to generate ACSs, such as line positions,

⁸ <https://www.hitran.org>

intensities, rotational and vibrational quantum assignments, electronic assignments, and also various pressure-broadening and pressure-shift values where available. The completeness and accuracy of line-lists are a key focus of both laboratory and *ab initio* studies. In this work, we use the latest version of line list data provided by the ExoMol group (Tennyson et al. 2020), summarized in Table 4.

3.6. Computational Details

We employ the ExoCross⁹ code developed by Yurchenko et al. (2018) to compute the temperature-dependent line strengths and the Voigt profile (Humlíček 1979) for every individual line under the conditions given in Table 5. We assume H/He broadening governed by background atmospheres composed of 85% H₂ and 15% He—typical Jovian-like atmosphere conditions. The spectral sampling resolution is optimized as a function of temperature, pressure, and spectral subdivisions in such a way as to fully resolve the individual lines.

4. RESULTS: ABSORPTION CROSS-SECTION

In this section, we present a brief discussion on the line-list source for each absorber, as well as illustrative examples of the pre-computed ACS data. Then, we compare our generated ACS data with the currently available database’s.

4.1. H₂O

Partridge & Schwenke (1997) used high-level *ab initio* approach to computing the potential energy surface and dipole moment function of water. They then empirically adjusted their water line list (hereafter, *PS97*) by comparing their line position with available laboratory spectra. About a decade later, the ExoMol team (Barber et al. 2006) computed the *BT2* water line list, which includes \sim twice as many transitions with a somewhat lower total angular quantum number J but over a wider spectral range, extending deeper into the blue-optical. However, the comparison of both line lists with laboratory H₂O measurements showed that the *PS97* ACSs are more accurate in predicting line positions than *BT2* at wavelengths longer than 1 μ m (Alberti et al. 2015; Melin & Sanders 2016). It is for this reason that the *PS97* list has been used in several works (e.g., Freedman et al. (2014); Marley & Robinson (2015)), despite more modern line lists. Meanwhile, HITEMP—the high-temperature arm of the CfA HITEMP database—was created, using a trimmed version

of the *BT2* line list, but with rigorous validation and adjustments against laboratory data (Rothman et al. 2010). Recently, ExoMol improved the *BT2* line list by refining the potential energy surfaces, and extending the wavelength range down to 0.25 μ m (40,000 cm^{-1}), referred to as the *POKAZATEL* (Polyansky et al. 2018) line list. Table 6 summarizes these line lists and their key differences, and Fig. 3 compares the resultant cross-sections for a representative pressure/temperature. Besides the spectral range, there are extensive differences in their line positions, line shifts with pressure, and the number of lines, clearly apparent in different spectral regions such as the 2.420–2.424 μ m band (K band)—subject to numerous high-resolution observations (e.g., Birkby et al. (2013)). Brogi & Line (2019) showed that these differences matter in constructing high-resolution spectroscopy cross-correlation functions potentially leading to bias in the interpretation of the atmospheric composition. Recently, Gandhi et al. (2020) compared the water *POKAZATEL* data with the laboratory HITEMP data, also in the context of high-resolution cross-correlation spectroscopy, showing very good agreement up to temperatures of \sim 1200 K.

In our ACS database, we used the *POKAZATEL* H₂O line list over the full spectral range of 0.25–100 μ m at the temperature and pressure conditions given in Table 5. Figure 4 shows a subset of our ACSs as a function of temperature.

More recently, Conway et al. (2020) have published their H₂O line list calculated from experimental spectroscopic data, which includes \sim 10⁶ transitions and it is limited up to $J_{max}=20$. Their line lists have shown a significant improvement in the line position for the ultraviolet spectral region. Note that the current ground-based telescopes with very high resolution are mostly detecting in the near-IR region; however, future telescopes in the UV-Vis regions are required to have accurate line positions for high-resolution cross-correlation modeling of observational data.

4.2. TiO

Several spectroscopic measurements have been carried out to determine the spectroscopic parameters such as electronic dipole moments, hyperfine spectral properties, and rotational and vibrational constants for the

⁹ github.com/Trovemaster/exocross/wiki

TiO electronic ground state¹⁰, $X^3\Delta$, as well as the low-lying excited states such as $B^3\Pi$, $C^3\Delta$, and $D^3\Pi$ (Steimle & Virgo 2003; Amiot et al. 1995; Balfour et al. 1993). In addition, several laboratory measurements have been done to determine the line position and strength between the following TiO electronic states: ($C^3\Delta - X^3\Delta$) (Hodges & Bernath 2018), ($c^1\Phi - a^1\Delta$) (Bittner & Bernath 2018), ($b^1\Pi - a^1\Delta$) (Ram et al. 1996; Bittner & Bernath 2018), ($A^3\Pi - X^3\Delta$) (Ram et al. 1999), ($f^1\Delta - a^1\Delta$) (Brandes & Galehouse 1985), and ($c^1\Phi - a^1\Delta$) (Bittner & Bernath 2018).

Kurucz (1992) collected the available laboratory spectroscopic data for all TiO transitions to make the first comprehensive laboratory TiO line list (hereafter TiO-*Kurucz92*). Concurrently, Plez et al. (1992) used a theoretical spectroscopic method to calculate the transition dipole moments to generate TiO opacities. A few years later, they used more accurate dipole moments from Langhoff (1997) as well as the available spectroscopic measured data to improve line positions and intensities of the TiO nine low-lying electronic states (Plez 1998).

Schwenke (1998) independently used *ab initio* methods that included the spin-orbit and rotation-orbit coupling to compute potential energy surfaces for 13 electronic states. These surfaces were used as a Rydberg-Klein-Rees (RKR) potential to extract rovibrational energy levels. Schwenke (1998) also adopted the transition moments from Langhoff (1997) to determine the intensities for each rovibrational transition in order to compute a complete line list (intensities and positions) for 45×10^6 lines. Allard et al. (2000) compared these two (Plez92 and Schwenke98) TiO line lists in the context of M- and Brown-dwarf atmospheres, finding that the Schwenke98 data could better model the thermal emission from cool substellar atmospheres.

Hoeijmakers et al. (2015) used Schwenke98 and Plez92 line lists to detect/identify TiO in the HD 209458b atmosphere via high-resolution cross-correlation spectroscopy ($R \approx 100,000$) finding that the line positions in both lists are not sufficient to extract an accurate signal. These mounting inadequacies in line positions and intensities motivated the need for a better,

more comprehensive, TiO line list. ExoMol used a high-quantum level of basis set computation methods with spin-orbit coupling to generate all rovibronic (rotation-vibration-electronic) transitions between the 13 low-lying electronic states, covering a spectral range of 0.33–100 μm (called *TOTO*, McKemmish et al. (2019a)). In our ACS database we used this *TOTO* line list¹¹ from 0.3-100 μm over the conditions given in Table 5. Figure 5 summarizes a subset of these ACSs and Figure 6 and 7 compare to past line lists using identical computational setups.

More recently, Bernath (2020a) have recorded the TiO spectra in the visible-near-infrared regions (476–1176 nm) at 2300 K, and compared the measured intensity and line position with the TOTO data. In addition, Nugroho et al. (2020) applied high-resolution cross-correlation spectroscopy method using the TiO Plez1998 (updated version) and *TOTO* line lists, but they could not detect TiO signature in KELT-20b atmosphere. Note that even though both Nugroho et al. (2020) and our study have used the same TiO-*TOTO* line list, our generated ACS data are different from their data because of the following reasons. First, their resolution is 100 points/wavenumber, however, our resolution is at least 1 times finer than them for several pressure-temperature points. Second, Their line wing cut-off is 100 cm^{-1} which is different from ours. Besides, our pre-generated ACS data covers a wider temperature and pressure range with larger grid points than the current pre-generated ACSs.

4.3. VO

Numerous laboratory works have focused on determining the spectroscopic constants of the ground-state ($X^4\Sigma^-$) and low-lying excited states, including the $A - X$ ($\sim 1.1 \mu\text{m}$ (Cheung et al. 1982)), $B - X$ ($\sim 0.74 \mu\text{m}$ (Huang et al. 1992)), and $C - X$ (~ 0.43 – $0.58 \mu\text{m}$ (Hopkins et al. 2009)) systems as well as quartet-quartet transitions (e.g., $^4\Delta - ^4\Pi$ and $^4\Delta - ^4\Phi$, ~ 0.85 and $1.05 \mu\text{m}$ (Merer et al. 1987)) and doublet-doublet transitions (e.g., $^2\Delta - ^2\Delta$ and $^2\Phi - ^2\Delta$, ~ 0.45 and $1.4 \mu\text{m}$ (Ram et al. 2002; Ram & Bernath 2005)). Complimenting the experiments, several theoretical *ab initio* works on VO have been undertaken to assign all rovibronic transitions to improve the atmospheric modeling of ultra-hot atmospheres (e.g., (Miliordos & Mavridis 2007)). Hübner et al. (2015) computed potential energy surfaces of the electronic ground and excited states and their corresponding spectroscopic constants

¹⁰ In diatomic spectroscopy, in general, the electronic ground state is represented by X and the higher electronic states are labeled by A , B , and so on. In addition, the electronic multiplicity ($2S+1$) and the total orbital angular momentum (Λ) are used to represent the electronic state. For example, $X^3\Delta$ is the ground state of TiO with a multiplicity of 3 and orbital angular momentum of Δ , which is equivalent to $\Lambda=2$. Hence, $C^3\Delta - X^3\Delta$ is showing the electronic transition between the TiO state C and X , with the same total orbital and spin angular momentums. Chapter 9 by Bernath (2005) provided detailed information on this topic.

¹¹ exomol.com/data/molecules/TiO/49Ti-16O/Toto/

(equilibrium radius, dissociation energies). McKemmish et al. (2016) (hereafter, *VOMYT*) improved upon these previous *ab initio* results by including spin-orbit and spin-spin couplings as well as by leveraging available spectroscopic data to modify the potential energy surface to improve line positions and intensities, resulting in a robust VO line list with 2.77×10^8 transitions. We used this *VOMYT* line list¹² to generate our VO cross-sections given the parameters in Table 5. A sample of these cross-sections is shown for multiple temperatures and pressures in Fig. 8. In addition, Fig. 9 illustrates the difference between the *VOMYT* ACS data with the old ones computed from the *Plez* and *Schwenke* line lists for the full UV-Vis-IR range. The reason for these considerable differences is due to the calculated number of transitions and the computed electronic states from each line list. For example, *Plez* (1999) has accounted for 3.1 million lines, while *VOMYT* has 277 million transitions, which explains why it has a higher ACS value. The number of transitions in the *Schwenke* line list is much smaller than *VOMYT* as shown in the figure. Further details can be found in table 19 by McKemmish et al. (2016).

4.4. FeH

FeH (iron monohydride) is a diatomic radical with a high-multiplicity ground state ($X^4\Delta$), resulting in a complex electronic spectrum (see page 71 in Veillard (2012)). Several laboratory spectroscopic measurements have been performed since the 1970s to record and analyze the FeH $F^4\Delta - X^4\Delta$ 0-0 band (known as Wing-Ford band) (McCormack & Oconnor 1976) as well as to characterize the infrared FeH spectra (Phillips et al. 1987a). Later, Dulick et al. (2003) used an *ab initio* quantum mechanic approach to calculate a new line list for several vibrational bands in the $F^4\Delta - X^4\Delta$ system, including the electronic transmission dipole moment and spectroscopic constants (e.g., rotation and vibration constants). Following their theoretical work, Wende, S. et al. (2010) used high-resolution spectroscopy to record the Wing-Ford spectral lines in 989.8–1076.6 nm. In the same year, Hargreaves et al. (2010) used the above laboratory data to investigate the $E^4\Pi - A^4\Pi$ ($\sim 1.58 \mu\text{m}$) rovibrational spectra. Note that the band strength of the $E - A$ system calculated from this work has been problematic in several astrophysical spectral observations, further discussed in §4.4.1, and so we did not include this $E - A$ band in generating our FeH opacities. More recently, (Bernath 2020b) synthesized these works into

the MoLLIST line database. We used the FeH line list by Dulick et al. (2003)¹³ to compute our cross-sections over the properties given in Table 5. Fig. 10 (left) illustrates a few pressure points from our grid and Fig. 10 (right) shows the results of including the Hargreaves et al. (2010) $E - A$ band.

4.4.1. Comments on FeH Line Lists

The history of the FeH line lists is complex and deserves an expanded discussion. Much of the uncertainty involves the $E^4\Pi - A^4\Pi$ electronic transition near $1.58 \mu\text{m}$ (6300 cm^{-1} , Fig. 10 (right panel)). Hargreaves et al. (2010) obtained the positions and intensities within this band using a spectrum previously recorded with a Fourier Transform Spectrometer at Kitt Peak National Observatory from an emission spectrum produced by a King-type furnace as the source (Phillips et al. 1987b). A calibration step was necessary to convert the measured emission intensities, without an absolute intensity scale, into line strengths at a given temperature, resulting in their line list for this $E - A$ transition.

However, there are several potential sources of uncertainty in this measured intensities-to-line strengths conversion. First, the temperature of the tube furnace was determined to be closer to 2200 K based on the relative line intensities (instead of the 2673 K as recorded by Phillips et al. (1987b)). The actual final calibration connecting the lab data to intensities was done using lines that had been individually identified by Balfour et al. (2004). The spread in the intensities (see Figure 1 in Hargreaves et al. (2010) paper) is quite large and a linear regression was used to obtain a conversion factor for the intensities. Hargreaves et al. (2010) mentioned in the paper that points used to calibrate the laboratory intensities contained considerable scatter, and the change in the assumed temperature may play a role in the intensity problem. In addition, An average lower state energy (2250 cm^{-1}) is used for all unassigned lines (96% of the lines provided), which would contribute to the uncertainty at temperatures away from 2200 K as the line list from this work was provided at 2200 K. Two points to note: the ratio of the partition function $Q(2673\text{K})/Q(2200\text{K}) = 1.64$ and the change in the factor needed to convert emission intensities to absorption values (see Eq. 6 in Hargreaves et al. (2010)) is approximately a factor of 2 when considering the ratio of the two temperatures. These caveats may play a role in

¹² exomol.com/data/molecules/VO/51V-16O/VOMYT/

¹³ exomol.com/data/molecules/FeH/56Fe-1H/MoLLIST/; Note that the reference given in the ExoMol website is mistakenly to the recent work by Wende, S. et al. (2010), but the provided line lists there are from Dulick et al. (2003).

astrophysical data-model comparisons, suggesting that this FeH band, in particular, deserves further theoretical and laboratory attention.

4.5. *TiH*

Several spectroscopic works have been performed to record and assign the TiH spectral systems including the $4\Gamma - X^4\Phi$ system (530 nm Steimle et al. (1991); Launila & Lindgren (1996)) and the vibrational $4\Phi - X^4\Phi$ system (938 nm (Andersson et al. 2003; Linton et al. 2012)) system. Burrows et al. (2005) re-investigate the previous TiH spectroscopy data in order to derive new spectroscopic constants to produce a line list, called MoLLIST. We employed this line-list¹⁴ to generate pre-computed ACS data over the parameters given in Table 5. Cross-sections for select pressures are shown in Fig. 11 (left).

4.6. *CrH*

An emission spectrum of the $A^6\Sigma^+ - X^6\Sigma^+$ (0.74–1 μm) system was first recorded by (Ram et al. 1993), later expanded upon by (Bauschlicher et al. 2001) who fit more bands (i.e., 1–0, 1–1, and 2–0) in the region of 0.67–1.11 μm . Recently, Bernath (2020b) combined them all these line-lists into the MoLLIST database. We used MoLLIST reformatted by the ExoMol group¹⁵ to generate ACS data for the available spectral range (i.e., 0.7–1.6 μm). Fig. 11 (right) shows our cross-sections as a function of pressure.

4.7. *CaH*

The infrared and electronic transitions of the ground state $X^2\Sigma^+$, excited states ($A^2\Pi$, $B^2\Sigma^+$, and $E^2\Sigma$, 0.45–1 and 2–14 μm respectively) have been characterized using high-resolution Fourier transform spectroscopy (Ram et al. 2011; Shayesteh et al. 2013). The Einstein-A-coefficients have also been calculated for these band systems (Li et al. 2012; Alavi & Shayesteh 2017a; Yadin et al. 2012). Additional *ab initio* investigations determined the transition dipole moments of the ground state $X^2\Sigma^+$, excited states (i.e., $A^2\Pi$, $B^2\Sigma^+$, and $E^2\Sigma$) (Shayesteh et al. 2017; Weck et al. 2003) covering wavelengths from 1–2 and 14–100 μm . Our cross-sections employs the laboratory-based lists synthesized by Bernath (2020b)¹⁶ over the 0.45–1 and 2–14 μm regions. For the remaining spectral range, i.e. 1–2 and 14–100 μm , we used the *ab initio* line list from Yadin

et al. (2012)¹⁷. Figure 12 (right) summarizes our cross-sections at 2000K over a range of pressures.

4.8. *MgH*

The spectroscopy of the ground state and low-lying excited electronic states of MgH has been the subject of numerous investigations. Balfour & Cartwright (1975a,b) and later Shayesteh & Bernath (2011) have measured the rovibronic transitions of the $A - X$ and $B' - X$ systems in order to extract line positions, dissociation energies, rotational constants, and their potential energy surfaces. Employing the latest potential energy surface's, Yadin et al. (2012) calculate all infrared transitions for the MgH ground electronic state for 1.2–100 μm . In addition, GharibNezhad et al. (2013) used high-resolution spectroscopic data to produce a line list from 0.35–1.2 μm . We compute our cross-section using the Yadin et al. (2012)¹⁸ line list from 1.2–100 μm and the GharibNezhad et al. (2013)¹⁹ from 0.35–1.2 μm . Figure 12(left) illustrates a slice on our cross-section grid for 2000K over a representative range in pressures.

4.9. *SiO*

Since the 1970s, SiO has been the subject of several spectroscopic studies over the UV-Vis to the IR using data recorded from both hot gas cells as well as the sunspots (Barrow & Stone 1975; Campbell et al. 1995; Sonnabend et al. 2006). Furthermore, the SiO potential energy surfaces, Einstein A coefficients, and other spectroscopic constants have been theoretically studied using *ab initio* method (Langhoff & Bauschlicher 1993; Langhoff & Arnold 1979). Later, as a part of the ExoMol initiative, Barton et al. (2013) improved the potential energy surface of the ground state and dipole moment function. In our calculation, we used the Barton et al. (2013) line list²⁰ to calculate cross-sections over 1.67–100 μm for the temperature and pressure range's reported in Table 5. Figure 13(right) shows a slice on our ACS grid for 2000 K over a representative range in pressures.

4.10. *AlH*

Different rovibronic lines of AlH have been measured in the lab using high-resolution spectroscopy, including the $A^1\Pi - X^1\Sigma^+$ band at 400–550 nm (Szajna & Zachwieja 2009; Ram & Bernath 1996), the $C^1\Sigma^+ - X^1\Sigma^+$

¹⁴ exomol.com/data/molecules/TiH/48Ti-1H/MoLLIST/

¹⁵ exomol.com/data/molecules/CrH/52Cr-1H/MoLLIST/

¹⁶ exomol.com/data/molecules/CaH/40Ca-1H/MoLLIST/

¹⁷ exomol.com/data/molecules/CaH/40Ca-1H/Yadin/

¹⁸ exomol.com/data/molecules/MgH/24Mg-1H/Yueqi/

¹⁹ exomol.com/data/molecules/MgH/24Mg-1H/MoLLIST/

²⁰ exomol.com/data/molecules/SiO/28Si-16O/EBJT/

band at 220–240 nm (Szajna & Zachwieja 2010). In addition, the AlH dissociation energy and the low-lying electronic states have been characterized using *ab initio* approach’s Matos et al. (1987). Recently, Yurchenko et al. (2018) employed these spectroscopic constants of the ground state and the first low-lying excited state, and experimental potential energy curves to calculate all rovibrational transitions between the energy levels. We employed their line list, named *WYLLoT*^{21,22}, to generate our ACSs from 0.4–100 μm for the temperature and pressure ranges in Table 5. Figure 13 (right) represents a subset of our ACSs as a function of pressure.

4.11. Comparison to Other Absorption Cross-Section Databases

There are other cross-section databases, some publicly available such as (Villanueva et al. 2018; Chubb et al. 2020), and some are not (Sharp & Burrows 2007; Freedman et al. 2008; Freedman et al. 2014; Goyal et al. 2018). We build on these past works by implementing the latest line lists, primarily drawn from the ExoMol, and provide an up-front description of our sources of pressure broadening and how we approach the problem when no data is available (see §3). Table 7 summarizes the known differences between our database and past absorption cross-section database’s. In summary, our database resolution is sufficiently large to be applicable for interpretation of *HST* and *JWST* observed data as well as high-resolution cross-correlations’. In addition, we used a constant number for the wing cut-off to avoid overestimation of the opacity continuum. The temperature, pressure, and wavelength ranges are also wider and have more grids (1460 T-P points) than other available pre-generated databases in order to fully model the (Ultra)Hot-Jupiters and M-L dwarf atmospheres.

5. IMPACT OF OPACITIES ON HIGHLY-IRRADIATED EXOPLANET ATMOSPHERES

We assess the impact of the newly generated ACSs on the atmospheres and spectra of M dwarfs and hot Jupiters—specifically, the influence of metal hydrides and oxides from EXOPLINES vs. Freedman2014 (Freedman et al. 2014) (see the list of the Freedman2014’s line lists at Table 2 by Lupu et al. (2014)). First, we simulate a representative Ultra-Hot Jupiter atmosphere ($T_{irr} \sim 2000$ K, $\log g = 3$, $T_{star} = 6500$ K, solar composition)

with a 1D-self-consistent radiative-convective thermochemical equilibrium model, Sc-CHIMERA²³, previously described in Piskorz et al. (2018); Arcangeli et al. (2018); Gharib-Nezhad & Line (2019). We compute the planetary emission and transmission spectrum from 0.3–5.0 μm . Major opacity sources included in these models are H₂O, TiO, VO, FeH, CO, CO₂, CH₄, NH₃, H₂S, HCN, C₂H₂, PH₃, CaH, MgH, CrH, SiO, AlH, Na, K, H₂–H₂, H₂–He, Fe, Mg, Ca, H- bound/free-free continuum, and H₂/He Rayleigh scattering within the correlated-K resort-rebin framework (Amundsen et al. 2016).

We illustrate the effects of TiO, VO, H₂O individually, and as combined with other metal hydrides (FeH, CaH, MgH, CrH, SiO, and AlH, with sources listed in Table 4). Figure 14 shows both transmission (left) and emission (right) spectra for an Ultra Hot Jupiter, varying only the choice of line list. Focusing first on the transmission spectrum, we report significant differences in the spectral shape below 1.0 μm ; however, in the near-infrared, the residual differences are well below 50 ppm²⁴. Between 0.3–1.0 μm , we find that major differences are due to the choice of TiO line list (TOTO vs. Schwenke, Freedman et al. (2014)), leading up to 320 ppm in residuals. Differences arising purely from the choice of metal hydride line lists (FeH, MgH, and CaH from MoLLIST), are around 75 ppm for the transmission spectrum, notably over wavelengths covered by the HST/WFC3 bandpass (1.4–2.0 μm). We also investigated the influence of H₂O line list choice on the transmission spectra, where we find residual differences fall under 10 ppm when comparing Schwenke (Freedman et al. 2014) to POKAZATEL.

For the thermal emission spectrum; similarly, TiO line list choice leads to significant differences in the spectral shape, especially from 1.0–5.0 μm , with up to 80 ppm differences. Metal hydrides and H₂O lead to residual differences around 10 ppm, also consistent with the transmission spectrum (see Figure 14). Moreover, the total differences between all old ACS data (e.g., TiO-Schwenke, VO-Plez, MgH-Weck, CaH-Weck, FeH-old) against the EXOPLINES ACS data (TiO-TOTO, VO-VOMYT, MgH-MoLLIST, CaH-MoLLIST, FeH-MoLLIST), are dominated by TiO and metal hydride line list differences, altogether leading up to the same level of residuals.

²¹ exomol.com/data/molecules/AlH/27Al-1H/AlHambra/

²² Although in the paper by Yurchenko et al. (2018), it was named as WYLLoT line list, the ExoMol website provided the AlH line list files with “AlHambra” name.

²³ The core radiative transfer, CHIMERA, found at <https://github.com/mrline/CHIMERA>

²⁴ *HST* WFC3 (1.1–1.4 μm) precision of 15–50 ppm are routinely achieved (Line et al. 2016; Kreidberg et al. 2014). Comparable or better precision are anticipated with *JWST* (Bean et al. 2018)

We also illustrated the impact of these new ACSs data on the Temperature-Pressure (TP-) profile of this candidate WASP-121b atmosphere in Fig. 15. This figure shows that the new TiO-TOTO ACS data change the TP profile by ~ 60 K between 1 mbar and 1 bar. The impact of all new molecular ACSs (TiO, VO, etc.) is ~ 130 K between 1 mbar to 1 bar. These differences in the TP-profile lead to change in the atmospheric chemical composition, emission, and transmission synthetic spectra.

More recently, Piette et al. (2020) showed that incorporating the different TiO opacities (i.e., TOTO, Plez, and Schwenke) biases the synthetic emission and transmission spectra of ultra-hot Jupiters ($R \sim 10^4$) up to ~ 1000 ppm in the visible and 100 ppm in the near-IR spectral region. In another instance for high-resolution ground-based spectroscopy, Herman et al. (2020) used TiO-Plez ACS to identify the potential presence of TiO optical lines in WASP-33b. Implications of these works strongly vouch for the critical vetting of line lists used to compute appropriate ACS, especially concerning oxygen-bearing molecules such as H₂O and TiO to robustly determine bulk chemical properties (such as C/O ratio) of sub-stellar atmospheres (Molaverdikhani et al. 2019), as well as improving the atmospheric circulation models of hot Jupiters (Kataria et al. 2016).

6. IMPACT OF OPACITIES ON M-DWARF ATMOSPHERES

M-dwarf atmospheric spectra are also subject to differences arising from various line lists. To quantify these differences, using the same self-consistent modeling framework described above, we simulate a dust-free $T_{\text{eff}} = 3000$ K, $\log g = 5$, solar composition atmosphere. In an upcoming paper by Iyer et al. (In Prep), we will discuss our M-dwarf model in great detail. Consistent with the hot Jupiter case, TiO line-list differences have the largest influence on the spectral shape and the temperature profile. We find that the TiO-TOTO (EXOPLINES) line-list alone, when compared to the Schwenke/Allard (Figure 16, left) produces spectral differences of up to 125%, primarily between 0.3–1.0 μm . Alternatively, the effect of VO opacity (Plez (Freedman et al. 2014) vs VOMYT (EXOPLINES)) and H₂O (Schwenke (Freedman et al. 2014) vs POKAZATEL (EXOPLINES)) do not contribute to any notable differences at lower resolutions ($R=100$), however, we see up to a 30% difference due to the effect of metal hydrides below 1 μm , and up to 12% over the near-IR (1.4–2.0 μm) bandpasses. TiO attributes to the largest variation in the temperature profile as well; (see Figure 16, right), with up to 50 K in differences between 1 mbar to 0.1 bar,

and up to 20 K difference deeper than 100 bars, because of a subtle shift in the adiabat. Furthermore, the absorption cross-sections from the hydrides (calculated from MoLLIST) lead to thermal profile differences of up to 10 and 20 K respectively, from 1 mbar to 0.1 bar and down to 100 bars. Undoubtedly, this level of bias—in both hot Jupiters and M-dwarfs—arising purely from generational differences of line lists would lead to improper atmospheric inferences. McKemmish et al. (2019b) also have recently investigated the impact of (Plez 1998), (Schwenke 1998), and TOTO TiO line lists on M-dwarf flux, which showed large differences in their synthetic flux.

7. CURRENT CHALLENGES WITH OPACITIES

Several spectroscopic parameters are critical for computing absorption cross sections and their subsequent effect in the modeling of observations (e.g., Fortney et al. 2019). Some challenges arise simply due to lack of laboratory data, and some are because of the computational shortcuts used to improve the speed of these often lengthy calculations. Therefore, it is crucial to consider these all differences between the Voigt profiles, broadening treatment, wing cut-off and other details in order to evaluate and cross-check different opacity databases generated by either CPU-based computing codes such as ExoCross and HAPI²⁵, or GPU-based codes such as Radis²⁶ and Helios-K²⁷ (Yurchenko et al. 2018; Kochanov et al. 2016; van den Bekerom & Pannier 2021; Grimm et al. 2021). We briefly discuss the current pressing challenges in producing accurate cross-sections:

- The Lack of Pressure Broadening Data—As discussed in §3, the pressure-broadening coefficients, γ_L and n_T , are critical to the proper computation of the Lorentz line widths and wings, which dictates the “off line” continuum. For an absorber, these coefficients depend on the broadening gas, quantum J number, molecular symmetry²⁸, temperature, and also the specific interactions with the broadening gas (e.g., the complexity in the line profile of Na and K atoms studied

²⁵ <https://github.com/hitranonline/hapi>

²⁶ <https://radis.readthedocs.io/en/latest/>

²⁷ <https://helios-k.readthedocs.io/en/latest/>

²⁸ Spectroscopic parameters such as pressure-broadening and molecular angular momentums (simply, quantum numbers) depend on the molecular geometry and the symmetry between different energy states. For example, CH₄ is a tetrahedral molecule and has A_1, A_1, F_1, F_2 and E symmetries, which can be found from character tables. For further details, check Table 3 by Rothman et al. (2005) and the discussion in chapter 3 by Bernath (2005). Several examples of broadening data can also be found in chapters 4 and 5 by Buldyreva et al. (2011).

by Allard et al. (2019, 2016)). The current state of broadening data for many molecules important in exoplanet/substellar atmospheres is concerning. In most cases for many absorbers γ_L measurements are limited to below 500 K (e.g., see review by Hartmann et al. (2018)). Most data are only applicable to “Earth-like” conditions through “air-broadening” or reducing solar-system giant-like atmospheres through H_2/He broadening. Regarding the metal hydrides and oxides in question, as far as our best knowledge, there is no laboratory/theoretical broadening data available..

- Compositional dependency of absorption cross sections: One of the key findings of the Kepler Mission is that a majority of exoplanets fall within this “warm mini-Neptune” regime ($R_p \sim 2-4R_{Earth}$ $T < 1000$ K) (Batalha 2014). The bulk composition of these exoplanets is not hydrogen-dominant, and therefore, incorporating the pre-generated H_2/He -broadened opacities to model their atmospheres may cause errors and biases in interpreting their observational emission and transmission spectra. For example, (Gharib-Nezhad & Line 2019) have shown that using the H_2/He -broadened of water opacity for modeling a candidate super-Earth steam atmosphere could lead up to 80 ppm (part-per-million) difference in transmission and 250 ppm in the emission spectra, which are detectable by both *HST* and the future *JWST* telescopes. As a result, there is uncertainty and inaccuracy in atmospheric modeling observables such as composition, which could lead to a misinterpretation of observational data.
- Line Profile—The Voigt profile is the most common line shape applied in opacity computations. This profile is based on the ideal gas assumption where no interactions between broadening (e.g., the bath gas/background) molecules exist. However, these interactions do occur, and hence, this effect should be taken into account with more advanced line profiles such as the speed-dependent Voigt profile (Pickett 1980; Buldyreva et al. 2011). These broadener gas interactions have been explored at both low and high pressures (Ngo et al. 2012; Grigoriev et al. 1999). Table 1 by Ngo et al. (2013) illuminates some of these differences.
- Voigt Profile Algorithm—The specific algorithm and inherent approximations used to compute the Voigt profile can result in non-negligible uncertainties. The Voigt algorithm by Humlíček (1979) is the most widely used due to the balance between accuracy and computational efficiency. However, it has been shown (Zaghloul 2015; Schreier 2018a) that this algorithm is not always accurate over the pressure, temperature, and wavelength regions. Other algorithms exist, but need to be continually assessed for accuracy in different situations (Schreier 2018b).
- Line Wing Cut-Off—This dictates the frequency extent to which the Lorentz line wings are computed from the line core—typically employed to reduce the computational burden. Choosing too short of a wing cut-off, particularly for high pressures (>10 bar), can result in large errors in the opacity continuum depending upon the number of transitions. Hartmann et al. (2002) proposed an empirical correction factor for the wing cut-off to fully model the $3.3 \mu\text{m}$ band of CH_4 , however, this study is only limited to room temperature and the broadener is H_2 molecule. Further investigations are required to understand the accurate wing cut-off for different line profiles.
- Intensity Cut-Off—This effectively limits the number of lines over which to compute the line strengths and profiles, and subsequent cross sections. Line intensities are typically given as the line strength at a particular reference temperature, usually 296K. Choosing a cut will remove the weaker lines that can present as stronger lines at higher temperatures, resulting in a critical loss in overall opacity. The cutoff choice is particularly influential with line lists that contain billions of transitions, which can result in the exclusion of a substantial portion of the weaker transitions, resulting in an altered “pseudo-continuum” shape. Figure 17 illustrates the impact of line-strength cut-off on the *POKAZATEL* H_2O cross-sections at 2000 K, 10^{-3} bar over the short wavelengths ($0.25 - 0.5 \mu\text{m}$).
- Pressure-shift— As a result of collision by the broadening gas, the line-center blue/red shifts by $\sim 0.001-0.005 \text{ cm}^{-1}/\text{bar}$, depending on the broadener, temperature, and quantum number J . At high pressures, lines extensively overlap due to their large line-width, but the line center will shift as well. To the best of our knowledge, this concept has not been applied in generating ACSs for the majority of absorbers (including the current study).
- Partition function— The strength of each individual line for different temperatures is scaled directly by the partition function, usually treated as a separate data source in opacity calculations. Partition function value for a given temperature is calculated from all the energy levels that have been obtained from spectroscopy measurements or through *abinitio* calculations (e.g., see equations by Barklem & Collet (2016) and Yurchenko et al. (2018)). Hence, incompleteness

or inaccuracy in the measured/computed energy levels results in errors in the partition function, and consequently in the computed line strengths, and resulting cross-sections. For example, the water partition function and its associated uncertainty have been studied by Vidler & Tennyson (2000). In addition, Sousa-Silva et al. (2014) have assessed the potential errors and challenges associated with calculating the PH_3 and NH_3 partition function values.

8. SUMMARY AND CONCLUSIONS

The major objective of this investigation is to provide a comprehensive pre-computed absorption cross-section database relevant to the spectral modeling of atmospheres of irradiated hot Jupiters and substellar objects. To this end, we present a public database of pre-computed molecular absorption cross-sections for all the isotopologues of MgH, AlH, CaH, TiH, CrH, FeH, SiO, TiO, VO, and H_2O . The pressure and temperature range of the grid span 10^{-6} –3000 bar and 75–4000 K, respectively (except H_2O which is 500–4000 K) and their spectral coverage vary depending on the availability of the line list data, typically covering 0.25–330 μm where possible.

We applied detailed care when determining the pressure broadening coefficients. Where available, we started from the published values estimated for the H_2/He broadening, or otherwise used a J -dependent collision theory. We described the history of the line lists of various species, and when possible compared the influence of available line lists on the absorption-cross sections. Finally, we determined the impact of line list choice (hence cross-sections) on the temperature structure and emergent spectra of a hot Jupiter and M-dwarf using a 1D self-consistent radiative-convective model. From the latter experiment we found that:

- The TiO-*TOTO* line list compared to the TiO-Schwenke line-list (and subsequent cross-sections) had the most significant influence on the thermal structures of the hot Jupiter ($\sim 60\text{K}$ differences) and a generic 3000 K M-dwarf (50 K differences). The resultant hot Jupiter spectra ($R=100$) differed between the two line-list scenarios of up to ~ 80 ppm in emission/secondary eclipse and ~ 320 ppm (near 0.3–1 μm) in transmission. The M-dwarf emergent spectra differed up to 125% over the wavelengths most influenced by TiO (0.3–1.0 μm).
- Considering the large differences in the number of transitions in the various H_2O line lists (see Table 6 and Fig. 3), the resulting differences in the emergent spectra and temperature structure were negligible

at these resolutions ($R=100$). However, at high resolution ($R>50,000$) these differences in line positions and intensities are more apparent and have been previously shown to influence molecular abundance determinations of transiting hot Jupiter’s using cross-correlation spectroscopy Brogi & Line (2019); Gandhi et al. (2020).

- The metal hydride (FeH, MgH, and CaH) cross-sections derived from the MoLLIST line-lists compared to past line lists (MgH-Weck, CaH-Weck) also result in notable differences in atmospheric observables, with up to an 80 K difference in the hot Jupiter temperature structure and 10 K in the M-dwarf. Differences in the hot Jupiter emission/transmission spectra approach ~ 50 ppm (around 1.4–2 μm). In the M-dwarf spectra, up to 45% change in flux occurs near 1.0 μm and 12% between 1.4–2.0 μm .

With the upcoming higher fidelity characterization of extra-solar planets and their hosts (e.g., M-dwarfs), accurate absorption cross section ingredients (line lists, broadening) are becoming increasingly critical to the success of properly estimating their atmospheric properties. We encourage the community to continue to invest resources in line list validation and vetting, *ab initio* and laboratory measurements of key broadening coefficients, and production and curation of vetted absorption cross-section databases.

9. SUPPLEMENTARY DATA

The pre-generated absorption cross-sections (ACS) data from this study are uploaded in ZENODO <https://zenodo.org/record/4458189>. Our full isotopologue-weighted binary database is approximately 0.5 Tb which includes 10 molecular sets of 1460 ACS temperature-pressure data with the size of $\sim 44\text{GB}$ per molecule. The un-weighted individual isotopologues ACS binary data are consist of 22 sets of molecular ACS data with 1460 temperature-pressure points for each and the total size of ~ 1 TB. The database will be available in multiple formats to suit various needs. First, we will post a 5 Gb resampled version of the database on Zenodo, due to their file size limitations. The Zenodo database will be in the same format as the (Freedman et al. 2014) database currently used by PICASO (Batalha et al. 2019; Batalha & Rooney 2020)²⁹. Second, the full unsampled database (MySQL format) will be available via an FTP-like portal. Last, we will also launch a web portal so that users can visualize and

²⁹ Zenodo Opacities (Freedman et al. 2014)

plot subsets of the data without needing to download it all.

10. ACKNOWLEDGEMENTS

EGN would like to thank Drs. J. Fortney, R. Lupu, I. Gordon, and R. Hargreaves for their useful comments and discussions during this study. EGN and ARI acknowledge Research Computing at Arizona State University for providing HPC resources that have contributed to the research results reported within this paper. EGN, MRL, and RF acknowledge support from HST-AR-15796. MRL and ARI acknowledge support from NASA grant NNX17AB56G. NEB and RF acknowledge support from 19-NUP2019-0011. We also acknowledge the ExoMol team for their continued production of large line lists and pertinent data critical to high-temperature atmospheric modeling. EGN's research was supported by an appointment to the NASA Postdoctoral Program at the NASA Ames Research Center, administered by Universities Space Research Association under contract with NASA. Finally, we thank the anonymous reviewers for their thoughtful comments.

11. SOFTWARE

We used the publicly available *ExoCross* code (Yurchenko et al. 2018) developed by the ExoMol group to generate the cross sections, and the CHIMERA radiative transfer and retrieval tool to produce the simulated emission/transmission spectra.

APPENDIX

A. APPENDICES

A.1. *Calculating the Lorentz coefficient (γ_L) based on collision theory*

The interaction between a given absorber with other atoms or molecules (i.e., perturbers) induces an extra width in the recorded spectral lines. In order to understand and calculate the line width, this interaction may be treated in two ways. The first approach is the classical approximation method in which the collision between the absorber and broadener occurs through a straight trajectory. The second method, however, uses quantum mechanical theory to describe the motion of perturbers. Limitations in both methods have been discussed in detail by [Baranger \(1958\)](#). In this study, we used Anderson theory which deals simultaneously with the motion of perturbers and the transition between energy levels with classical and quantum mechanics ([Anderson 1949](#)). The total energy in the system is then solved through perturbation theory, and the collisional half-width of the spectral line can be represented by Eq. A1 (see Eq. 28 by [Anderson \(1949\)](#)):

$$\Delta\nu_{\frac{1}{2}} = \frac{1}{2\pi} n_b \bar{v}_{th} \sigma_{col} \quad (\text{A1})$$

where n_b is the number density of perturbers, \bar{v}_{th} is the mean relative velocity of the gas ($=\sqrt{8k_B T/\mu\pi}$), and σ_{col} is the collision cross-section in \AA^2 unit. Using the gas kinetic theory, HWHM linewidth $\Delta\nu_{1/2}$ (in Hz/Pa) may be written as:

$$\Delta\nu_{\frac{1}{2}} = \left(\frac{8k_B T}{\mu\pi}\right)^{1/2} \frac{1}{2k_B\pi} T^{-1/2} \sigma_{col} p_b \quad (\text{A2})$$

where k_B is a Boltzmann constant and μ is the reduced mass of the colliding pair in atomic mass unit ($\mu = M_{absorber} M_{broadener} / (M_{absorber} + M_{broadener})$), and p_b is the partial pressure of the broadening gas. Comparing Eq. A2 to Eq. 2 shows that $\Delta\nu_{\frac{1}{2}}$ is equivalent to Lorentz HWHM (Γ_L) (see Eq. 36c and its related discussion by [Baranger \(1958\)](#)). By converting the unit of Eq. A2 to $\text{cm}^{-1}/\text{atm}$ and $\text{cm}^{-1}/\text{bar}$, the Lorentz coefficient γ_L can be written as:

$$\gamma_L[\text{cm}^{-1}/\text{atm}] = 0.0567 (T\mu)^{-1/2} \sigma_{col} \quad (\text{A3})$$

or,

$$\gamma_L[\text{cm}^{-1}/\text{bar}] = 0.0574 (T\mu)^{-1/2} \sigma_{col} \quad (\text{A4})$$

in which, the temperature dependence of the $\gamma_L(T)$ is:

$$\gamma_L(T) = \gamma_L(T_0) \left(\frac{T}{T_0}\right)^{-1/2} \quad (\text{A5})$$

Note that this equation can only provide a rough estimate of the pressure-broadening coefficients because the accuracy of the results relies on the collision cross section and also kinetic theory to provide the temperature-dependence coefficient of -1/2.

Table 1. Available calculated/estimated Lorentz coefficient, $\gamma_{L,b}[\text{cm}^{-1}/\text{atm}]$ from the literature (for Eq. 2).

Absorber	Broadener	$\gamma_{L,b}(J=0)^*$	$\gamma_{L,b}$	Reference
H ₂ O	H ₂	0.09	laboratory data	Ba17
H ₂ O	He	0.02	laboratory data	Ba17
TiO, VO	H ₂	0.1	$0.1 - 0.002J_{\text{lower}}$ **	Sh07
TiO, VO	He	0.06	$0.06 - 0.0012J_{\text{lower}}$	
FeH, TiH, CrH	H ₂	0.075	$0.075 - 0.001J_{\text{lower}}$	Du03,Bu02,Bu05
FeH, TiH, CrH	He	0.045	$0.045 - 0.0006J_{\text{lower}}$	

* $\gamma_{L,b}$ is reported for $J=0$ and 296 K. For H₂O, we adopted the J -dependency proposed in the cited studies. The J -dependency of other molecules is discussed in §3.3.

** Note, this equation was mistakenly proposed to provide a FWHM of γ_L by Sharp & Burrows (2007), but in fact, it is for calculating the HWHM value.

References: Ba17: The H₂O Lorentz coefficients were collected by the ExoMol group <http://exomol.com/data/molecules/H2O/>, and was discussed by Barton et al. (2017); Bu05: (Burrows et al. 2005); Bu03: (Burrows et al. 2002); Du03: (Dulick et al. 2003); Sh07: Sharp & Burrows (2007).

Table 2. Collision cross-section used to calculate the Lorentz pressure-broadening coefficient, $\gamma_{L,b}[\text{cm}^{-1}/\text{atm}]$

Absorber	Broadener	μ	σ_{col}	$\gamma_{L,b}$	Reference
$^{24}\text{Mg}^1\text{H}$	H_2	1.85	NA	0.08	$=\gamma_L(\text{CaH-H}_2)$
$^{24}\text{Mg}^1\text{H}$	He	3.45	NA	0.05	$=\gamma_L(\text{CaH-He})$
$^{40}\text{Ca}^1\text{H}$	H_2	1.91	NA	0.08	$=1.6\gamma_L(\text{CaH-He})$
$^{40}\text{Ca}^1\text{H}$	He	3.64	~ 27	0.05	[1]
$^{27}\text{Al}^1\text{H}$	H_2	1.87	NA	0.08	$=\gamma_L(\text{CO-H}_2)$
$^{27}\text{Al}^1\text{H}$	He	3.50	NA	0.05	$=\gamma_L(\text{CO-He})$
$^{28}\text{Si}^{16}\text{O}$	H_2	1.91	~ 20	0.05	[2]
$^{28}\text{Si}^{16}\text{O}$	He	3.67	~ 10	0.02	[3]

Notes:

1. The reported $\sigma_{col} [\text{\AA}^2]$ is the excitation collision cross section (for $J = 0 \rightarrow 1$ in most cases) for collision kinetic energy calculated for 296 K ($E_{kin} = (4k_B T/\pi) \approx 5.2 \times 10^{-21} \text{Joule} = 262 \text{ cm}^{-1} = 0.032 \text{ eV}$).
 2. The calculated $\gamma_{L,b}$ is used to calculate HWHM Lorentz width, $\Gamma_{L,b}$ in Eq. 2.
 3. $\gamma_{L,b}$ is reported at temperature 296 K for $J=0$. §3.3 discusses its J -dependency.
 4. In the case of AlH-H₂ and AlH-He systems, we used CO Lorentz coefficients because they both have a very close dipole moment and reduced mass.
 5. In a case of MgH, CaH, and SiO molecules, we used this assumption of $\gamma_{L,b}(\text{He})=0.6\gamma_{L,b}(\text{H}_2)$.
- Reference: [1](Akpınar & Akbalık 2010), [2](Yang et al. 2018), [3](Dayou, F. & Balança, C. 2006).

Table 3. Fitted coefficients of the Fourth-order Padé formula (see Eq. 4) to provide $\gamma_L[\text{cm}^{-1}/\text{atm}]$ for J quantum numbers up to 500.

Absorber	Broadener	a_0	a_1	a_2	a_3	b_1	b_2	b_3	b_4
AlH	H ₂	7.6101e-02	-4.3376e-02	1.9967e-02	2.4755e-03	-5.6857e-01	2.7436e-01	3.6216e-02	1.5350e-05
AlH	He	4.8630e-02	2.1731e+03	-2.5351e+02	3.8607e+01	4.4644e+04	-4.4438e+03	6.9659e+02	4.7331e+00
CaH, MgH	H ₂	8.4022e-02	-8.2171e+03	4.6171e+02	-7.9708e+00	-9.7733e+04	-1.4141e+03	2.0290e+02	-1.2797e+01
CaH, MgH	He	5.0424e-02	-1.1014e+02	2.2833e+01	2.8527e-01	-2.4407e+03	5.5472e+02	-3.4490e+01	6.5808e+00
CrH, FeH, TiH	H ₂	7.0910e-02	-6.5083e+04	2.5980e+03	-3.3292e+01	-9.0722e+05	-4.3668e+03	6.1772e+02	-2.4038e+01
CrH, FeH, TiH	He	4.2546e-02	-3.0981e+04	1.2367e+03	-1.5848e+01	-7.1977e+05	-3.4645e+03	4.9008e+02	-1.9071e+01
SiO	H ₂	4.7273e-02	-2.7597e+04	1.1016e+03	-1.4117e+01	-5.7703e+05	-2.7774e+03	3.9289e+02	-1.5289e+01
SiO	He	2.8364e-02	-6.7705e+03	2.7027e+02	-3.4634e+00	-2.3594e+05	-1.1357e+03	1.6065e+02	-6.2516e+00
TiO, VO	H ₂	1.0000e-01	-2.4549e+05	8.7760e+03	-8.7104e+01	-2.3874e+06	1.6350e+04	1.7569e+03	-4.1520e+01
TiO, VO	He	4.0000e-02	-2.8682e+04	1.0254e+03	-1.0177e+01	-6.9735e+05	4.7758e+03	5.1317e+02	-1.2128e+01

Notes:

1. See §3.3 for a detailed discussion regarding the calculation of these Fourth-order Padé coefficients.
2. These coefficients were used to compute the pre-generated absorption cross-sections in this study.

Table 4. Summary list of opacities: molecules, temperature, pressures, and their line lists (see §3.5 & 4).

Absorber	Line list	λ [μm]	No. Lines	P [bar]	T [K]	PT points	I_{cutoff}	Abundance(%)	Reference
$^{26}\text{Al}^1\text{H}$	WYLLoT	0.4-330	3.6×10^4	10^{-6} -3000	75-4000	1460	10^{-50}	0.00	Yu18
$^{27}\text{Al}^1\text{H}$	WYLLoT	0.4-330	3.6×10^4	10^{-6} -3000	75-4000	1460	10^{-50}	100.00	Yu18
$^{27}\text{Al}^2\text{H}$	WYLLoT	0.4-330	3.6×10^4	10^{-6} -3000	75-4000	1460	10^{-50}	0.00	Yu18
$^{40}\text{Ca}^1\text{H}$	MoLLIST	0.45-1, 2-14	1.9×10^4	10^{-6} -3000	75-4000	1460	10^{-50}	96.93	All17,Li12
$^{40}\text{Ca}^1\text{H}$	Yadin	1-2, 14-330	2.7×10^4	10^{-6} -3000	75-4000	1460	10^{-50}	96.93	Ya12
$^{52}\text{Cr}^1\text{H}$	MoLLIST	0.7-1.6	1.4×10^4	10^{-6} -3000	75-4000	1460	10^{-50}	83.78	Bu02
$^{56}\text{Fe}^1\text{H}$	MoLLIST	0.37-330	1.2×10^5	10^{-6} -3000	75-4000	1460	10^{-50}	91.74	We10
$^{24}\text{Mg}^1\text{H}$	MoLLIST	0.35-1.2	3.1×10^4	10^{-6} -3000	75-4000	1460	10^{-50}	78.99	Gh13
$^{24}\text{Mg}^1\text{H}$	Yadin	1.2-330	6.7×10^3	10^{-6} -3000	75-4000	1460	10^{-50}	78.99	Ya12
$^{25}\text{Mg}^1\text{H}$	Yadin	1.2-330	6.7×10^3	10^{-6} -3000	75-4000	1460	10^{-50}	10.00	Ya12
$^{26}\text{Mg}^1\text{H}$	Yadin	1.2-330	6.7×10^3	10^{-6} -3000	75-4000	1460	10^{-50}	11.01	Ya12
$^{28}\text{Si}^{16}\text{O}$	EBJT	1.67-330	1.8×10^6	10^{-6} -3000	75-4000	1460	10^{-50}	92.00	Ba13
$^{28}\text{Si}^{17}\text{O}$	EBJT	1.67-330	1.8×10^6	10^{-6} -3000	75-4000	1460	10^{-50}	0.03	Ba13
$^{28}\text{Si}^{18}\text{O}$	EBJT	1.67-330	1.8×10^6	10^{-6} -3000	75-4000	1460	10^{-50}	0.19	Ba13
$^{29}\text{Si}^{16}\text{O}$	EBJT	1.67-330	1.8×10^6	10^{-6} -3000	75-4000	1460	10^{-50}	4.67	Ba13
$^{30}\text{Si}^{16}\text{O}$	EBJT	1.67-330	1.8×10^6	10^{-6} -3000	75-4000	1460	10^{-50}	3.08	Ba13
$^{48}\text{Ti}^1\text{H}$	MoLLIST	0.4-2	2.0×10^5	10^{-6} -3000	75-4000	1460	10^{-50}	73.71	Bu05
$^{46}\text{Ti}^{16}\text{O}$	TOTO	0.3-330	3.0×10^7	10^{-6} -3000	75-4000	1460	10^{-50}	8.22	Mc19
$^{47}\text{Ti}^{16}\text{O}$	TOTO	0.3-330	3.0×10^7	10^{-6} -3000	75-4000	1460	10^{-50}	7.42	Mc19
$^{48}\text{Ti}^{16}\text{O}$	TOTO	0.3-330	3.0×10^7	10^{-6} -3000	75-4000	1460	10^{-50}	73.54	Mc19
$^{49}\text{Ti}^{16}\text{O}$	TOTO	0.3-330	3.0×10^7	10^{-6} -3000	75-4000	1460	10^{-50}	5.40	Mc19
$^{50}\text{Ti}^{16}\text{O}$	TOTO	0.3-330	3.0×10^7	10^{-6} -3000	75-4000	1460	10^{-50}	5.17	Mc19
$^{51}\text{V}^{16}\text{O}$	VOMYT	0.28-330	2.8×10^8	10^{-6} -3000	75-4000	1460	10^{-50}	99.5	Mc16
$^1\text{H}_2^{16}\text{O}$	POKAZATEL	0.25-100	1.1×10^9	10^{-6} -300	500-4000	1460	10^{-34}	99.75	Po18

Notes:

1. We used a single line list for some molecules such as TiO, SiO, and H₂O. For some molecules such as CaH and MgH, multiple line lists were used in order to compute opacity data for the full spectral range. See §3.5 and §4 for more details on the line lists.

2. Species are weighted according to their solar/natural elemental abundances provided by NIST database: www.nist.gov/pml/atomic-weights-and-isotopic-compositions-relative-atomic-masses.

3. For each species, absorption cross section data are provided in two ways: separate for each isotopologues and weighted based on their natural abundance.

References: All17=Alavi & Shayesteh (2017b), Bu02=Burrows et al. (2002) Ba13=Barton et al. (2013), Bu05=Burrows et al. (2005), Gh13=GharibNezhad et al. (2013), Li12=Li et al. (2012), Mc19=McKemmish et al. (2019b), Mc16=(McKemmish et al. 2016), Po18=Polyansky et al. (2018), We10=Wende, S. et al. (2010), Ya12=Yadin et al. (2012), Yu18=Yurchenko et al. (2018)

Table 5. Opacity computational details

Absorbers:							
H ₂ O	TiO	VO	SiO	CaH			
MgH	AlH	TiH	CrH	FeH			
Broadeners* : 85% H ₂ + 15% He							
T[K] grid: (73 points)**							
75	100	110	120	130	140	150	160
170	180	190	200	210	220	230	240
250	260	270	275	280	290	300	310
320	330	340	350	375	400	425	450
475	500	525	550	575	600	650	700
750	800	850	900	950	1000	1100	1200
1300	1400	1500	1600	1700	1800	1900	2000
2100	2200	2300	2400	2500	2600	2700	2800
2900	3000	3100	3200	3300	3400	3500	3750
4000							
P[bar] grid: (20 points)							
10 ⁻⁶	3×10 ⁻⁶	10 ⁻⁵	3×10 ⁻⁵	10 ⁻⁴	3×10 ⁻⁴		
10 ⁻³	3×10 ⁻³	10 ⁻¹	3×10 ⁻¹	10 ⁻²	3×10 ⁻²		
1	3	10	30	100	300		
1000 3000							
Wing cutoff:†							
P>200 bar: 150 cm ⁻¹							
P≤200 bar: 30 cm ⁻¹							
Opacity code: ExoCross(Yurchenko et al. 2018)							
Voigt Algorithm: Humlíček (1979)							

*These broadening mixture is a good choice for hydrogen-dominated atmospheres such as (Ultra) hot-Jupiters and M dwarfs. For high metallicity atmospheres such as super-Earths and mini-Neptunes, better choice of broadeners such as H₂O and CO₂ is essential.

** For H₂O molecule, absorption cross-sections are calculated for temperature range 500–4000K.

†To compute the line-profile and include the effect of pressure-broadening, Lorentz profile is used. The calculation of Lorentz profile for each individual line can be extended to the full spectral range or be limited to a few wavenumbers. This is one main challenge in computing opacities, and some studies such as (Hartmann et al. 2002) and (Bézard et al. 2011) have shown the non-Lorentzian behavior of the line profile. See §7 for more discussion.

Table 6. Comparing different H₂O line lists.

Line Lists	Method	λ [μm]	J_{max}	No. Lines	Note	Ref.
PS97	<i>ab initio</i>	0.4 – 100	55	$\sim 3 \times 10^8$	more accurate than BT2 for $\lambda > 1$	[1]
BT2	<i>ab initio</i>	0.33 – 100	50	$\sim 5 \times 10^8$	more transition than Ames1997, shorter wavelength	[2]
POKAZATEL	<i>ab initio</i>	0.25 – 100	72	$\sim 1 \times 10^9$	higher intensity than BT2 at $\lambda < 1 \mu\text{m}$	[3]
HITEMP	lab/ <i>ab initio</i>	0.33 – 100	50	$\sim 1 \times 10^8$	included strong BT2 lines and experimental lines*	[4]

* After rigorous assessment of the impact of the BT2 intensity at 296–4000K, Rothman et al. (2010) have kept only 25% of the BT2 lines (see their Eq. 2 and their criteria for different wavenumber ranges and temperatures).

Ref.: [1] (Partridge & Schwenke 1997), [2] (Barber et al. 2006), [3] (Polyansky et al. 2018), [4] (Rothman et al. 2010)

Table 7. Summary of the current opacity databases for the molecules in our investigation.

Abs. Cross Sec.	Linelist	λ [μm]	T[K]	P[bar]	Points/ cm^{-1}	P-T Pairs	Wing cut-off [cm^{-1}]
H₂O							
EXOPLINES	POKAZATEL	0.25–100	500–4000	10^{-6} –300	50–120	486	100–300
Gandhi2020*	POKAZATEL	0.95–5	400–1600	10^{-5} –10	100	49	Not reported
Malik2019**	BT2	0.5–20	50–2900	10^{-6} – 10^3	100	812	100
Goyal2018†	BT2	0.33–100	70–3000	10^{-9} – 10^3	1000	800	100
MacDonald2019‡	POKAZATEL	0.4–50	100–3500	10^{-6} – 10^2	100	162	30
Freedman2014††	Schwenke	0.5–100	75–4000	10^{-6} –300	80–120	1060	25–250
Chubb2020‡‡	POKAZATEL	0.3–50	100–3400	10^{-5} –100	2–75	594	10–500
TiO							
EXOPLINES	TOTO	0.3–100	75–4000	10^{-6} –3000	2–285	1460	30,150
Malik2019	Plez/Schwenke	0.5–5	50–2900	10^{-6} – 10^3	100	812	100
Goyal2018	Plez	0.3–100	70–3000	10^{-9} – 10^3	1000	800	100
MacDonald2019	TOTO	0.4–50	100–3500	10^{-6} – 10^2	100	162	30
Freedman2014	Schwenke/Allard	0.32–100	75–4000	10^{-6} –300	80–120	1060	25–250
Chubb2020	TOTO	0.3–50	100–3400	10^{-5} –100	2–75	594	10–500
VO							
EXOPLINES	VOMYT	0.28–100	75–4000	10^{-6} –3000	2–285	1460	30,150
Malik2019	VOMYT	0.5–20	50–2900	10^{-6} – 10^3	100	812	100
Goyal2018	VOMYT	0.3–100	70–3000	10^{-9} – 10^3	1000	800	100
MacDonald2019	VOMYT	0.4–50	100–3500	10^{-6} – 10^2	100	162	30
Freedman2014	Plez	0.8–100	75–4000	10^{-6} –300	80–120	1060	25–250
Chubb2020	VOMYT	0.3–50	100–3400	10^{-5} –100	2–75	594	10–500
FeH							
EXOPLINES	Dulick	0.37–100	75–4000	10^{-6} –3000	2–285	1460	30,150
Goyal2018	Wende2010	0.67–50	70–3000	10^{-9} – 10^3	1000	800	10
MacDonald2019	Wende2010	0.4–50	100–3500	10^{-6} – 10^2	100	162	30
Freedman2014	Dulick/Hargreaves	0.37–100	75–4000	10^{-6} –300	80–120	1060	25–250
Chubb2020	Wende2010	0.3–50	100–3400	10^{-5} –100	2–75	594	10–500
MgH							
EXOPLINES	MoLLIST/Yadin	0.35–100	75–4000	10^{-6} –3000	2–285	1460	30,150
Malik2019	Yadin	1.2–20	50–2900	10^{-6} – 10^3	100	812	100
MacDonald2019	MoLLIST/Yadin	0.4–50	100–3500	10^{-6} – 10^2	100	162	30
Freedman2014	Weck	0.3–2.5	75–4000	10^{-6} –300	80–120	1060	25–250
Chubb2020	Wende2010	0.3–50	100–3400	10^{-5} –100	2–75	594	10–500
AlH							
EXOPLINES	WYLLoT	0.4–100	75–4000	10^{-6} –3000	2–285	1460	30,150
Malik2019	WYLLoT	0.4–20	50–2900	10^{-6} – 10^3	100	812	100
MacDonald2019	WYLLoT	0.4–50	100–3500	10^{-6} – 10^2	100	162	30
Chubb2020	WYLLoT	0.3–50	100–3400	10^{-5} –100	2–75	594	10–500
CaH							
EXOPLINES	MoLLIST/Yadin	0.45–100	75–4000	10^{-6} –3000	2–285	1460	30,150
Malik2019	Yadin	1–20	50–2900	10^{-6} – 10^3	100	812	100
MacDonald2019	Yadin	1–50	100–3500	10^{-6} – 10^2	100	162	30
Freedman2014	Weck	0.8–2.5	75–4000	10^{-6} –300	80–120	1060	25–250
Chubb2020	MoLLIST	0.3–50	100–3400	10^{-5} –100	2–75	594	10–500

*Gandhi2020=Gandhi et al. (2020) ACSs data were generate to be used for calculating cross-correlation function for high-resolution exoplanet spectroscopy.

**Malik2019=Malik et al. (2019) ACS data have been used to model the irradiated exoplanets. The pressure grid used for the opacities goes from 10^{-6} bar to 10^3 bar with a logarithmic step size of 1/3 dex, that makes 28 pressure points. The temperature grid goes from 50 K to 2900 K with a linear step size of 50 K between 50 K and 700 K, a step size of 100 K between 700 K and 1500K, and a step size of 200 K between 1500 K and 2900 K. That is 29 temperature points in total. Opacities above 3000 K were extrapolate.

†Goyal2018=Goyal et al. (2018) ACS data have been used in **ATMO** code for modeling forward exoplanet spectra.

‡MacDonald2019=MacDonald (2019) (see chapter 5) ACS data are a part of **POSIEDON** database for atmospheric retrievals.

††Freedman2014=(Lupu et al. 2014; Freedman et al. 2008; Freedman et al. 2014) were used in **Exo-Transmit** and **PICASO** code (Kempton et al. 2017; Batalha et al. 2019) to model transmission, emission, and reflected exoplanetary atmospheric spectra.

‡‡Chubb2020=Chubb et al. (2020): In this work, the resolving power is 15,000 and the wing cut-off is $500 \times \gamma_{\text{Voigt}}$. In comparison, our resolution is 2–20 times larger in order to fully and accurately could be employed in modeling *JWST*- and high-resolution cross-correlation technique. Our wing cut-off is also a constant number of 30 and 150 cm^{-1} because the real shape of Voigt profile is non-Lorentzian and using a very large number can lead to an intensive overestimation of the opacity continuum.

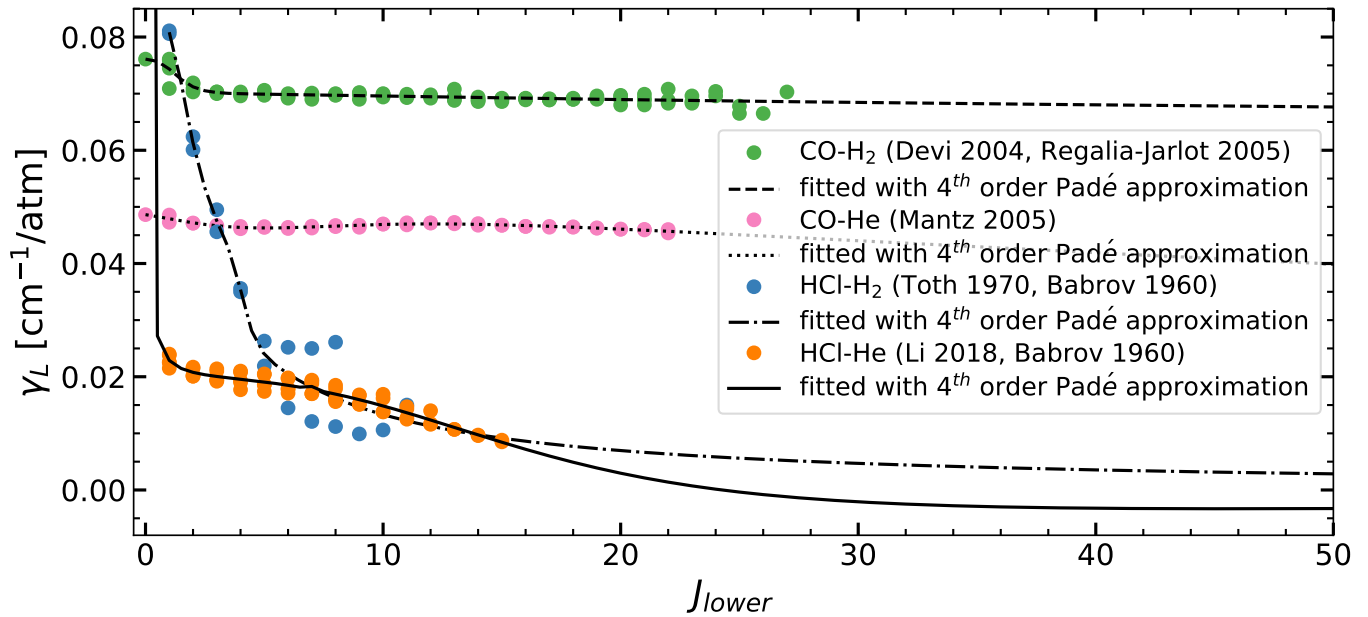


Figure 1. Comparison of H₂ and He-broadening Lorentz HWHM of CO and HCl molecules using laboratory data. HCl-H₂ system has much stronger J -dependency than CO-H₂, which could be due to their difference in their dipole moments. In contrast, the J -dependency of He is lower in both cases. The black lines are also showing the fitted data with 4th order Padé equation (Eq. 4). Since this equation could go to negative values in some systems and a very large number for $J=0$ (such as HCl-He case), we applied additional limitation (see Eq. 5). We used Eq. 4 to calculate the J -dependency of AlH, MgH, CaH, SiO, TiH, FeH, and CrH (see Fig. 2). Data of CO and HCl systems in this plot is collected from (Devi et al. 2004; Régalia-Jarlot et al. 2005; Mantz et al. 2005; Toth et al. 1970; Li et al. 2018; Babrov et al. 1960) (see §3.3 for more details.).

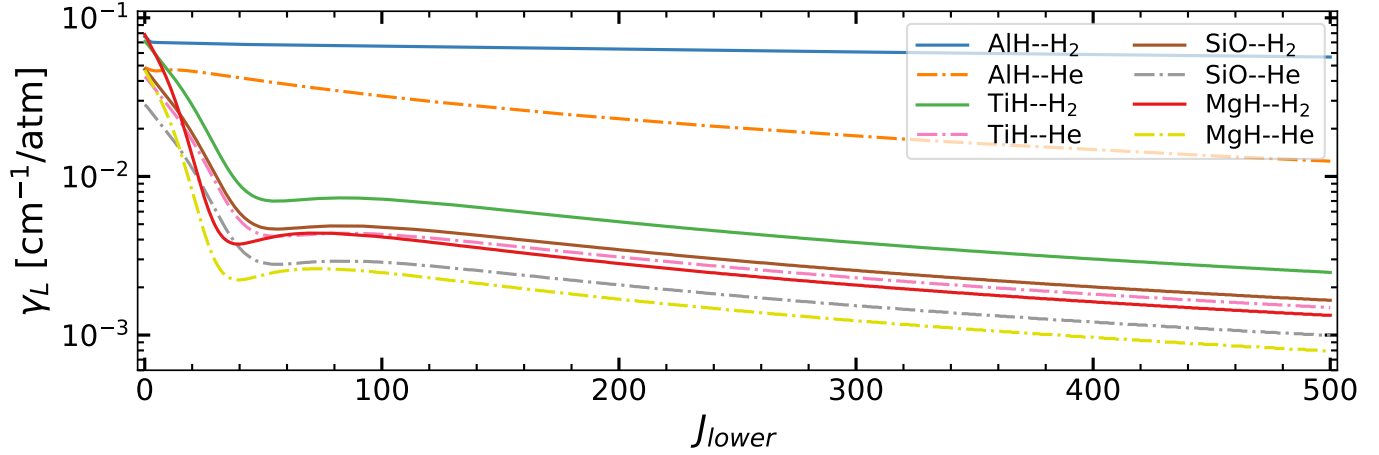


Figure 2. Example of used Lorentz coefficients for AlH, TiH, SiO, and MgH. The AlH Lorentz coefficients are assumed to be equal to CO, because they both have the same dipole moments. For other absorbers, the Lorentz coefficient are decreasing sharply up to $J=40$ similar to HCl because they all have high dipole moments. 4^{th} order Padé equation (Eq. 4 including the constrains introduced in (Eq. 5) is used and the coefficients are reported in Table 3 in order to reproduce these broadening data (see §3.3 for more details.).

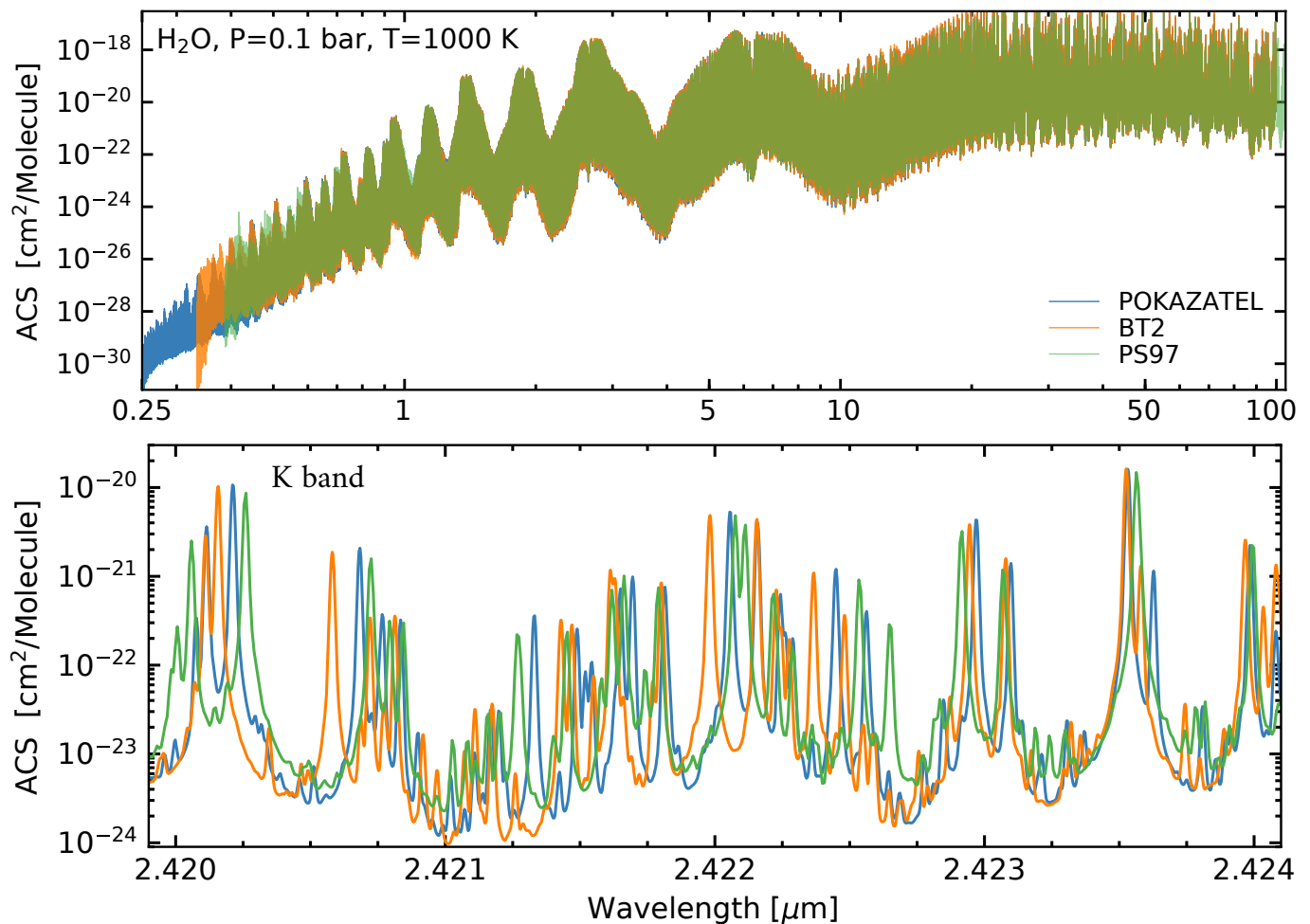


Figure 3. Comparison of different H₂O ACS for 0.1 bar and 1000K, including POKAZATEL, BT2, and PS97. Note, that *POKAZATEL* and *BT2* line lists are from ExoMol group, however, *POKAZATEL* is the most recent version. In addition, the Schwenke ACS is generated by [Freedman et al. \(2014\)](#) using [Partridge & Schwenke \(1997\)](#) water line list (named *PS97*). Their expanded comparisons for 2.4 μm (bottom) shows some differences in their line positions, intensities. Additionally, there are some extra lines from POKAZATEL that are not exist in others. Although they are weak, but they can change the opacity continuum, and so their inclusion is important in particularly windows spectral regions (see 7 for more discussion). These differences result from the implemented quantum mechanic level of complexity, and they could bias the interpretation of medium-to-high-resolution observed data.

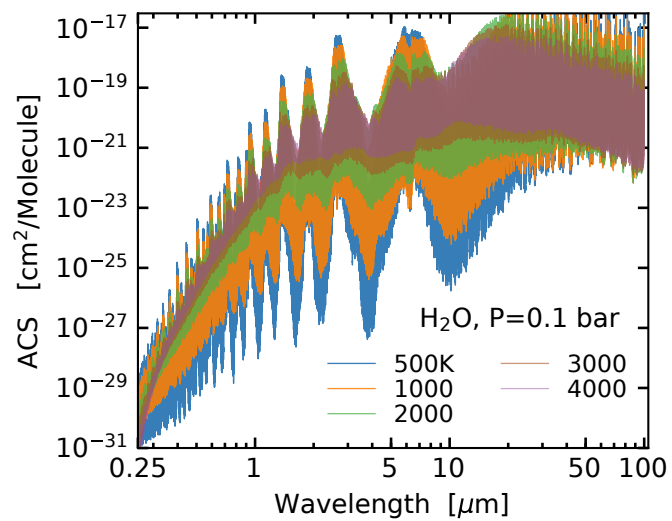


Figure 4. Example of H₂O *POKAZATEL* ACS spectra for 0.1 bar and multiple temperatures. For the same pressure, ACS with higher temperature have broader Doppler linewidth, and this will results in larger opacity in the line core comparing to the wings.

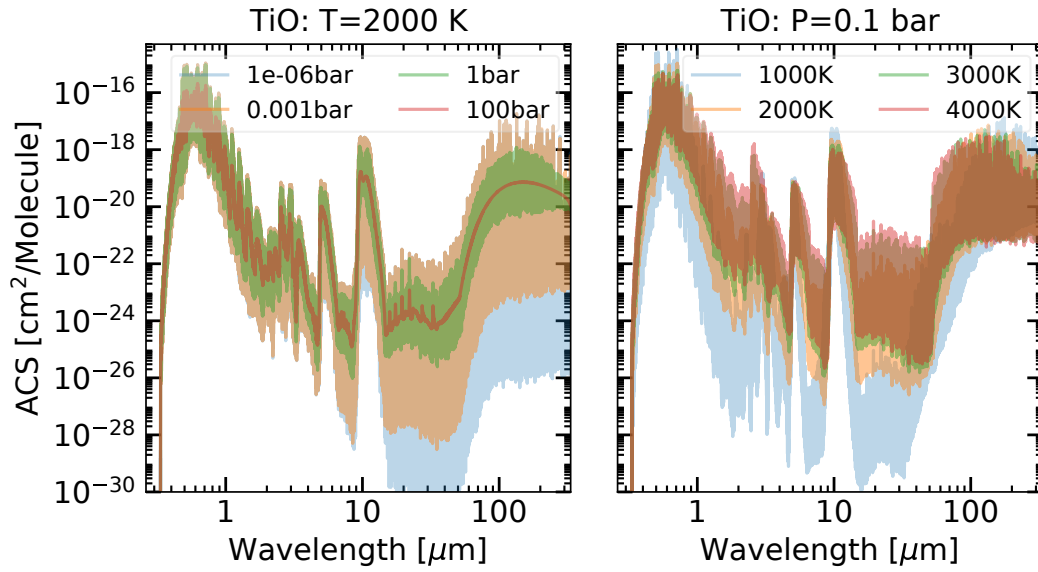


Figure 5. Example of the pre-generated TiO-*TOTO* ACS data: at a constant pressure, Doppler effect is the main source of line-width, particularly at low wavelengths (right). In contrast, at constant temperature, the higher pressure shows the most broadening as a result of collisional effect (left). Note that Lorentz width is dependent on the temperature as well. We used (McKemmish et al. 2019b) line list to generated these ACS data.

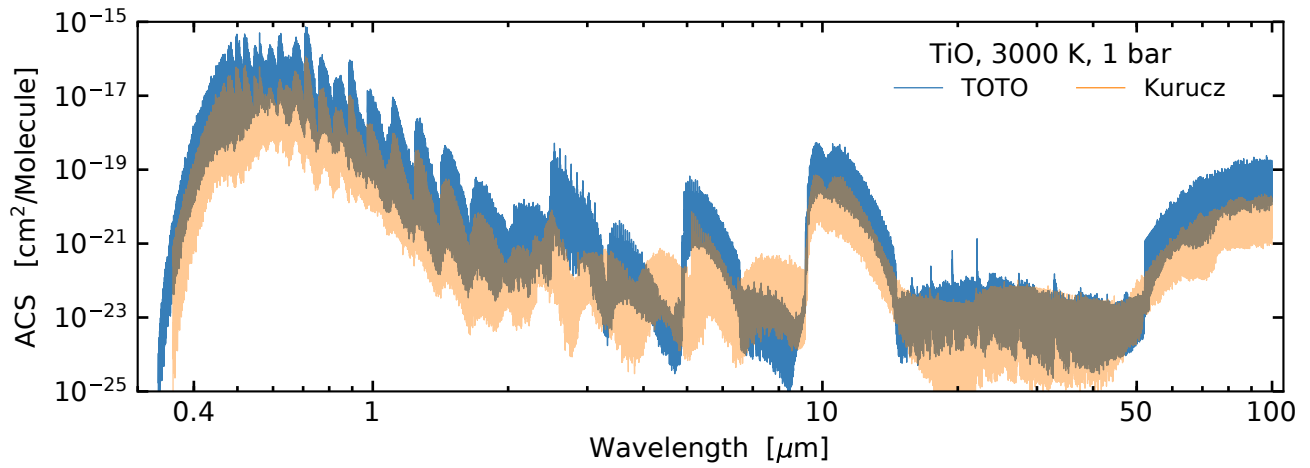


Figure 6. Compare TiO absorption cross-sections generated from *TOTO* and *Kurucz* line list for 1 bar and 3000 K. Note that there are noticeable differences in the whole spectral range between both cases. 2.5–9 μm region is showing the highest inconsistency between two spectra. Overall, the TiO *TOTO*-ACS is showing a larger value than the Kurucz data, which might be due to its large number of transitions as well as the modified electronic states which results in shift in some spectral bands.

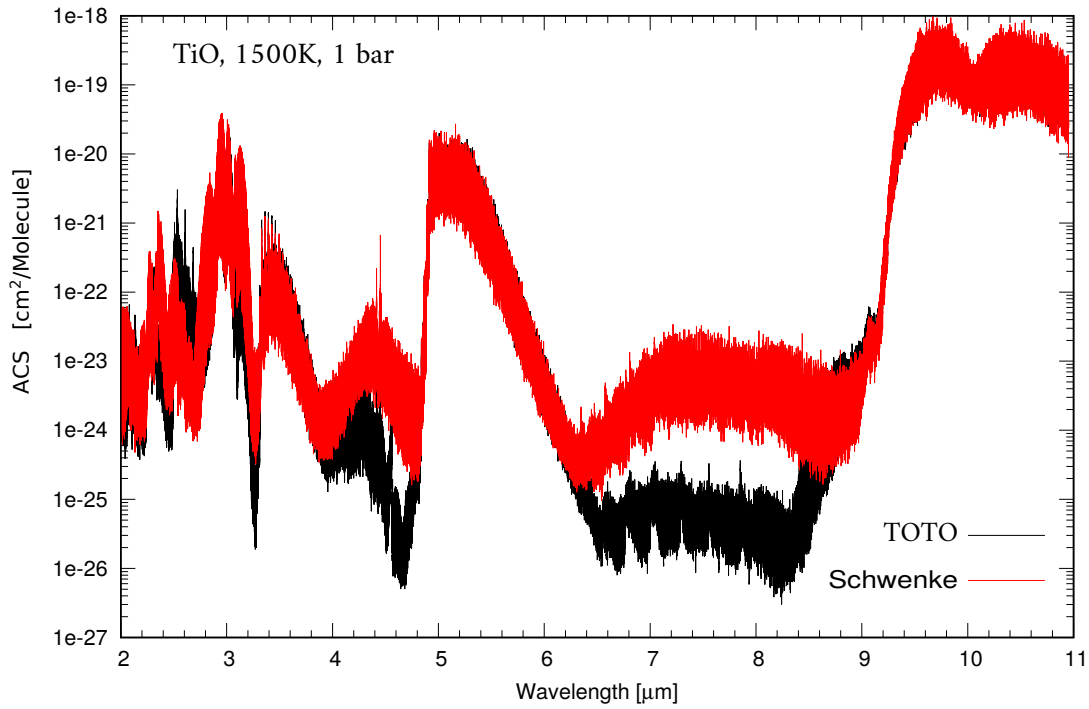


Figure 7. Compare TiO absorption cross-sections generated from the *TOTO* and *Schwenke* line list for 1 bar and 1500 K. There are noticeable differences in the whole spectral range between both cases. The highest inconsistency is at spectral regions $\sim 4\text{--}5$ and $6.5\text{--}8.5$ μm , that results in a dramatic bias in modeling low and high resolution synthetic emission or transmission spectra. One possible explanation would be the difference between the number of rotational levels that have been accounted by both *TOTO* and *Schwenke* linelist.

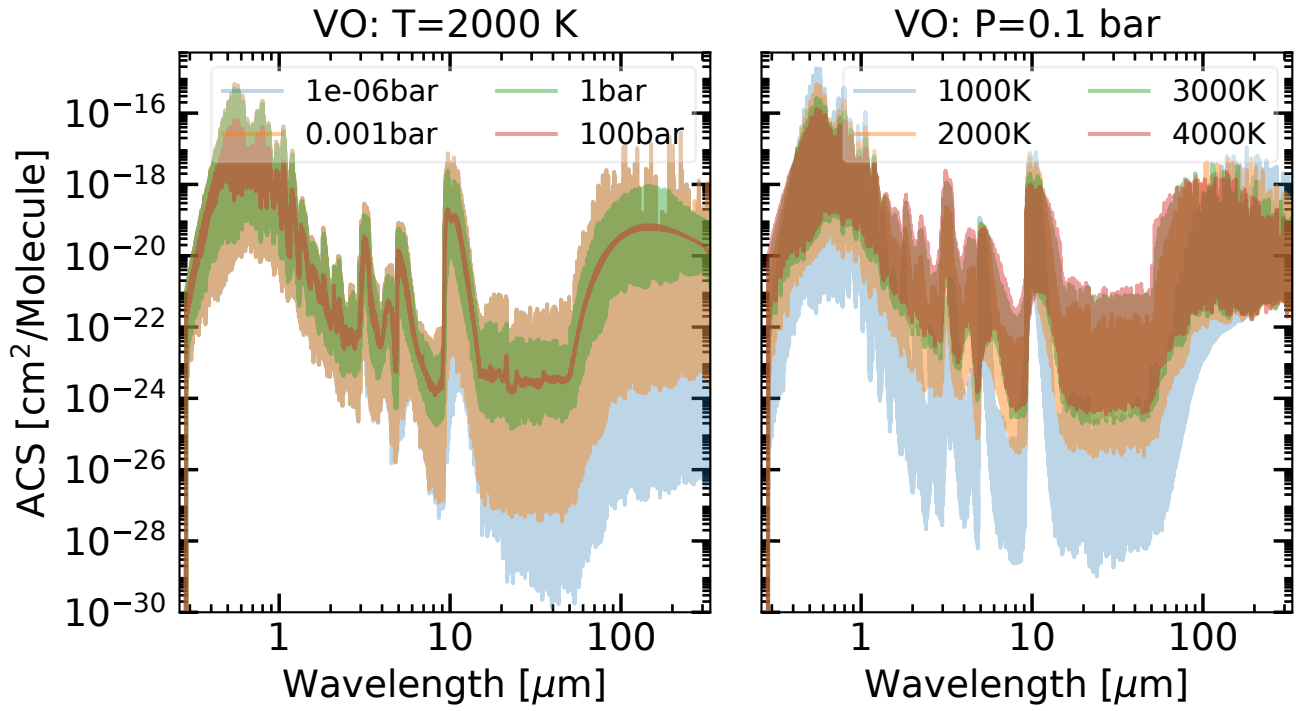


Figure 8. Example of our pre-generated VO-VOMYT absorption cross-sections: at a constant pressure, Doppler effect is the main reason of controlling the line-width, particularly at low wavelengths (right). In contrast, at constant temperature, the higher pressure shows the most broadening as a result of collisional effect (left). These pre-generated ACSs are from (McKemmish et al. 2016) line list data, which consists of the 13 low-lying electronic state and have ~ 227 million lines.

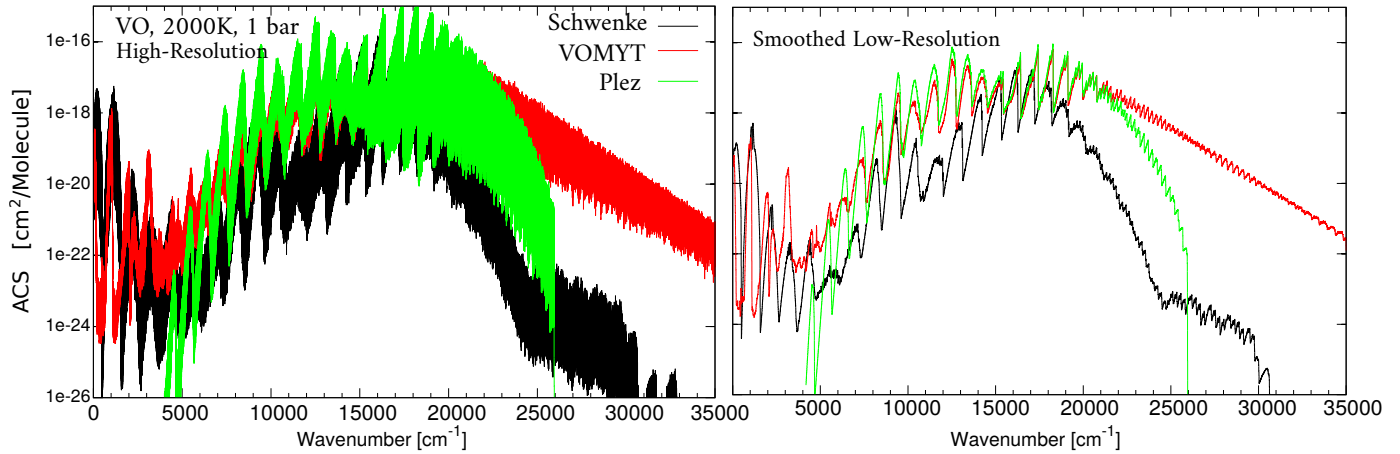


Figure 9. Comparison of different VO absorption cross-sections generated from different line lists: *Schwenke*, *VOMYT*, and *Plez* at 2000 K and 1 bar. *VOMYT* line list (McKemmish et al. 2016) includes the 13 low-lying states and ~ 227 million transitions, and hence the intensity of its spectra (red) is higher than other line lists (except *Plez* around 10000 cm^{-1} which resulted from A–X transitions). In contrast, *Plez* line list (Plez 1999)(green) has only the A–X, B–X, and C–X bands with no infrared transitions, and so it is only showing data at $5000\text{--}25000\text{ cm}^{-1}$ ($0.4\text{--}2\text{ }\mu\text{m}$). The central message of this figure is to show the difference between VO-ACS data from different line lists is remarkable, and naive implementation of VO ACS data could result in false conclusions and misinterpretation of the observational exoplanet/brown-dwarf spectra.

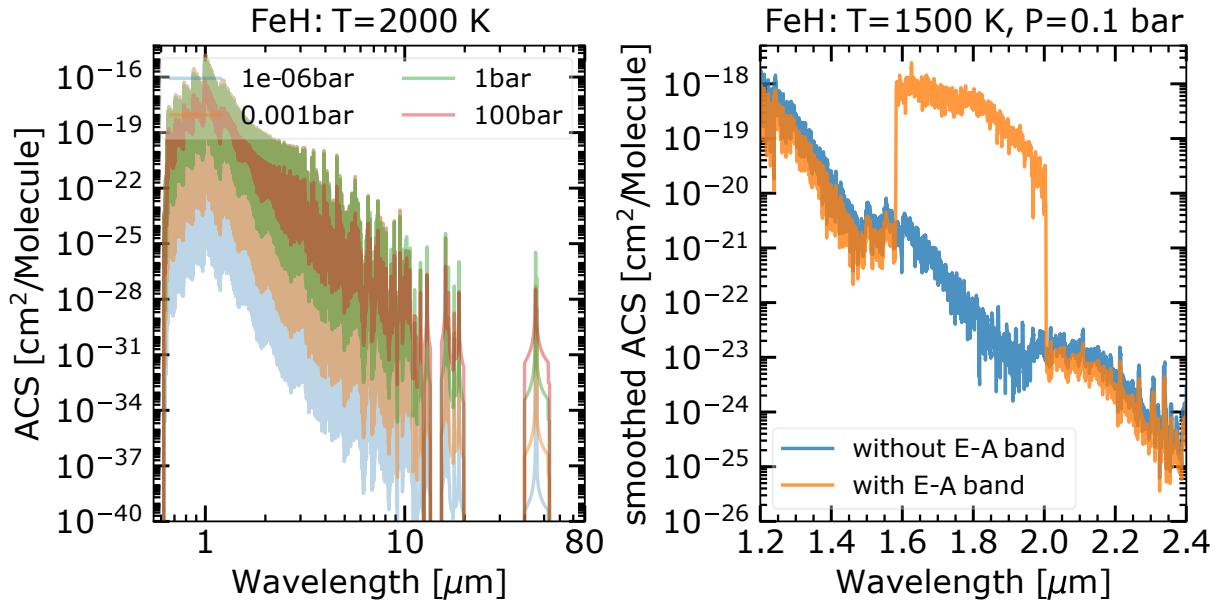


Figure 10. (left) An example of our FeH ACS spectra generated from [Dulick et al. \(2003\)](#) linelist for multiple pressures and 2000 K. (right) Comparison of the FeH absorption cross-sections generated with (orange) and without (blue) including the $E - A$ band. The discrepancies in these ACS data are due to the lack of sufficient accuracy in the $E - A$ band.

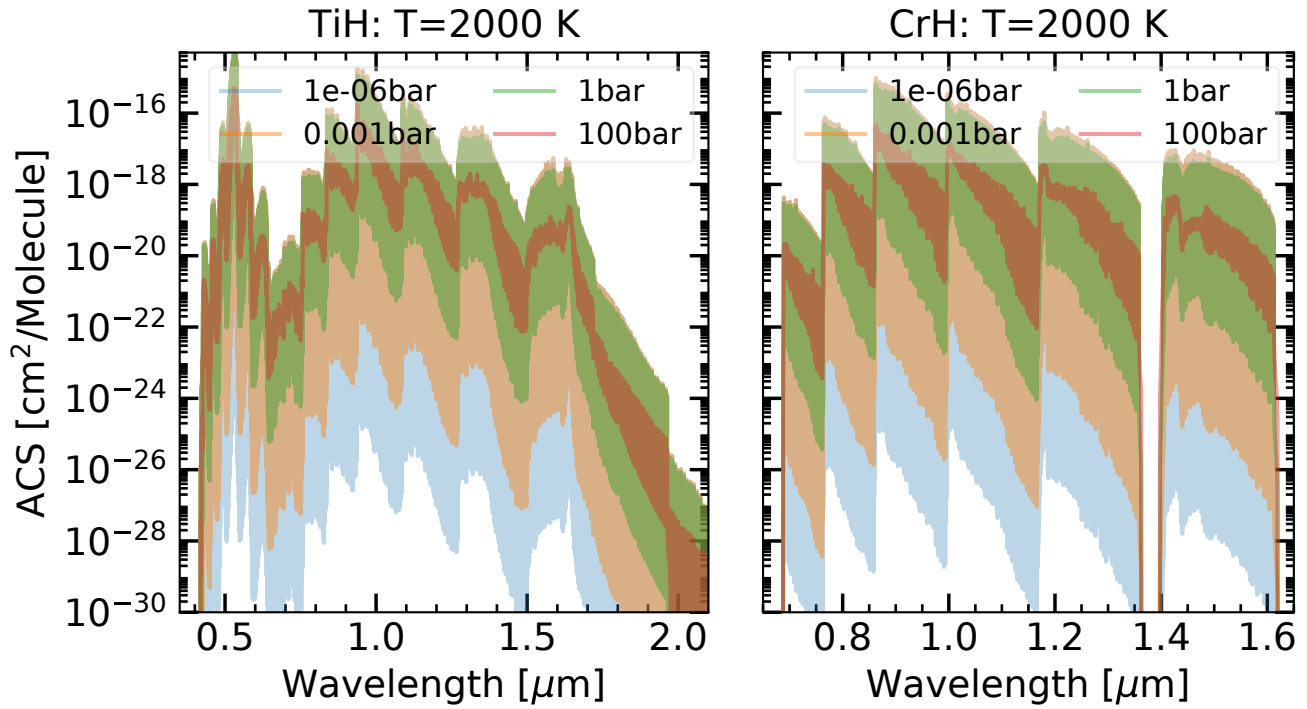


Figure 11. Example of our pre-generated TiH (left) and CrH (right) absorption cross-sections data at 2000 K, and multiple pressures. The TiH line list have been generated using a combination of *ab initio* data as well as spectroscopic measurements for 0.4–2.1 μm (A–X and B–X systems) by Burrows et al. (2005). The CrH line lists are also used from Burrows et al. (2002) for 0.65–1.65 μm (A–X system). These line lists are limited to these wavelength range, and future laboratory/*ab-initio* studies are needed to extend these spectra to higher wavelengths (e.g., for CrH at 1.38 μm gap).

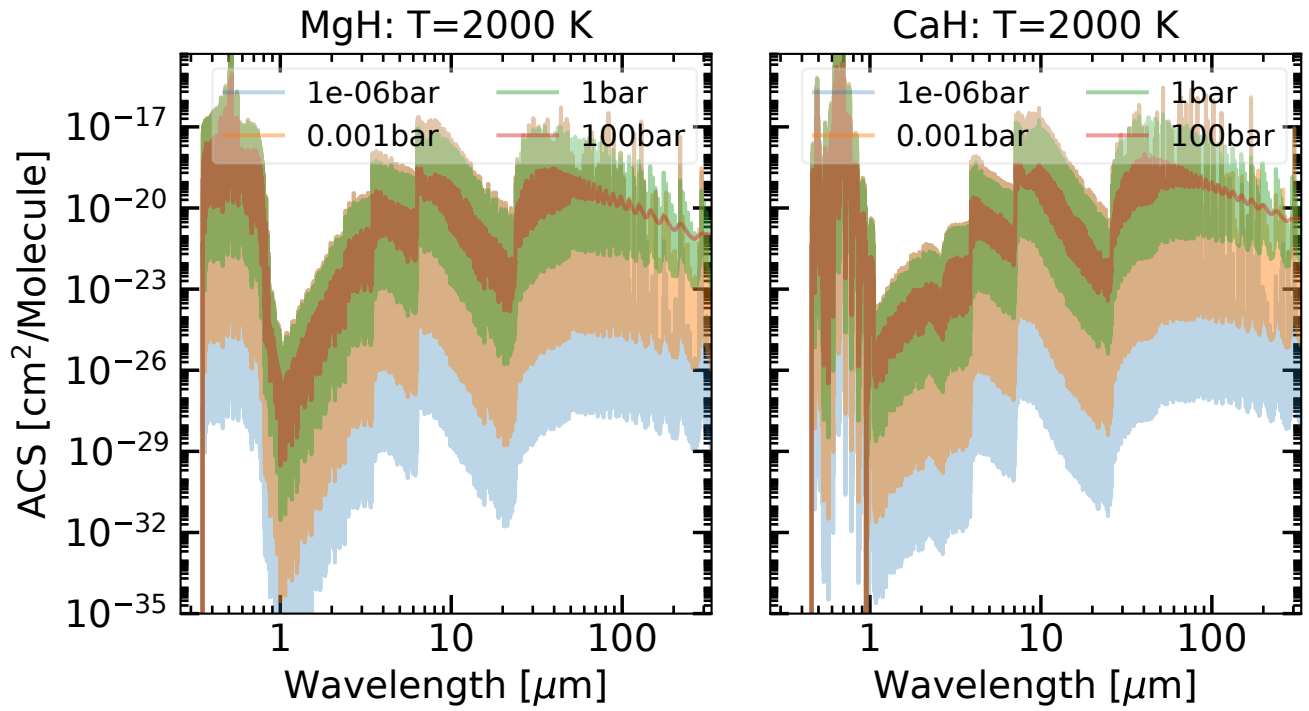


Figure 12. Example of our pre-generated MgH (left) and CaH (right) absorption cross-sections data at 2000 K, and multiple pressures. The generated MgH is a combination of the laboratory line list from [GharibNezhad et al. \(2013\)](#) for $0.35\text{--}1.2\mu\text{m}$ ($A-X$ and $B-X$ transitions) as well as theoretical infrared line lists from [Yadin et al. \(2012\)](#). The CaH includes laboratory measured line lists from [Alavi & Shayesteh \(2017b\)](#); [Li et al. \(2012\)](#) for $0.45\text{--}1.0$ ($A-X$ and $B-X$), $0.7\text{--}11$ (rovibrational transitions) by [Shayesteh et al. \(2004\)](#), and the μm ($E-X$) transitions $\sim 0.48\mu\text{m}$ by [Li et al. \(2012\)](#). CaH is also consists of theoretical line list generated by ([Yadin et al. 2012](#)) for rovibrational transitions. See Table 4 for further details.

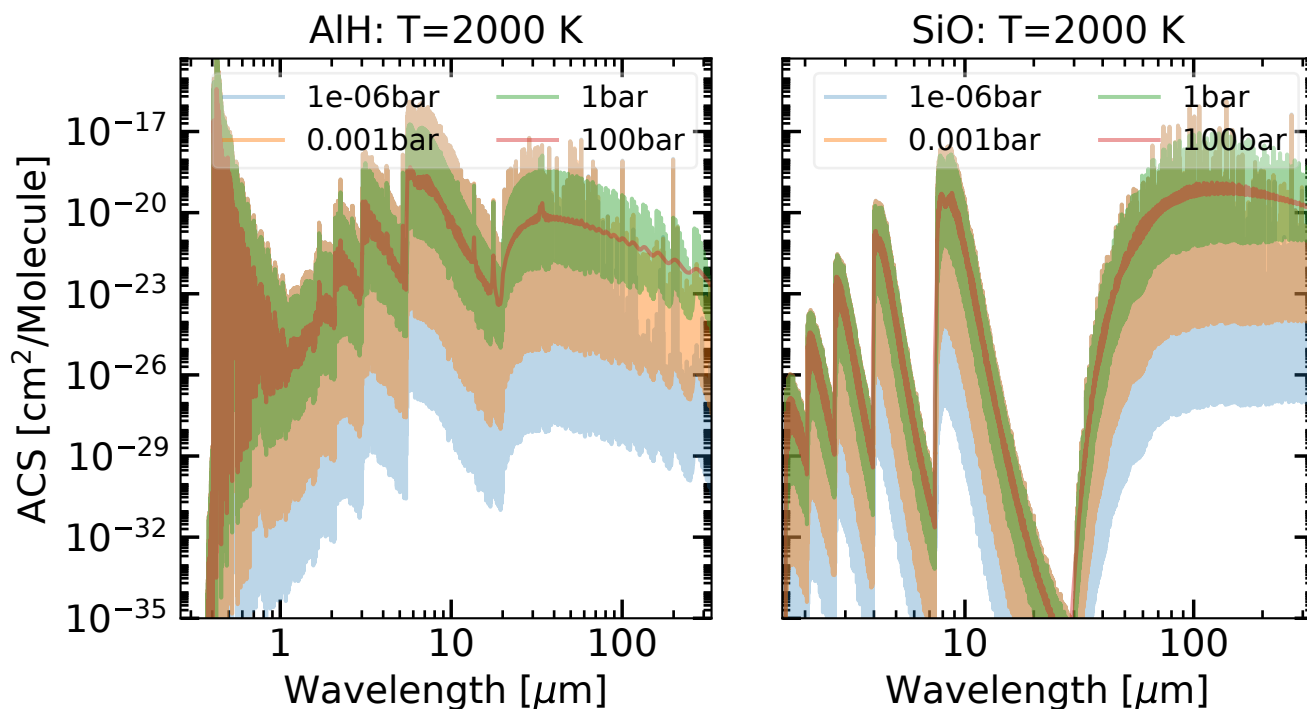


Figure 13. Example of our pre-generated AlH (left) and SiO (right) absorption cross-sections data at a 2000 K and multiple pressures. The AlH line list (named WYLLoT) is obtained from experimentally-calculated electronic states of X and A by Yurchenko et al. (2018) and so consists of $A-X$ and $X-X$ transitions. On the other hand, the SiO line list in our study has been computed using the available recorded SiO from both laboratory and sunspot spectra as well as the computed dipole moments by Barton et al. (2013). According to Barton et al. (2013), the SiO lines above 10000 cm^{-1} are very weak and so any lines between $10000\text{--}65000\text{ cm}^{-1}$ was filtered in their study.

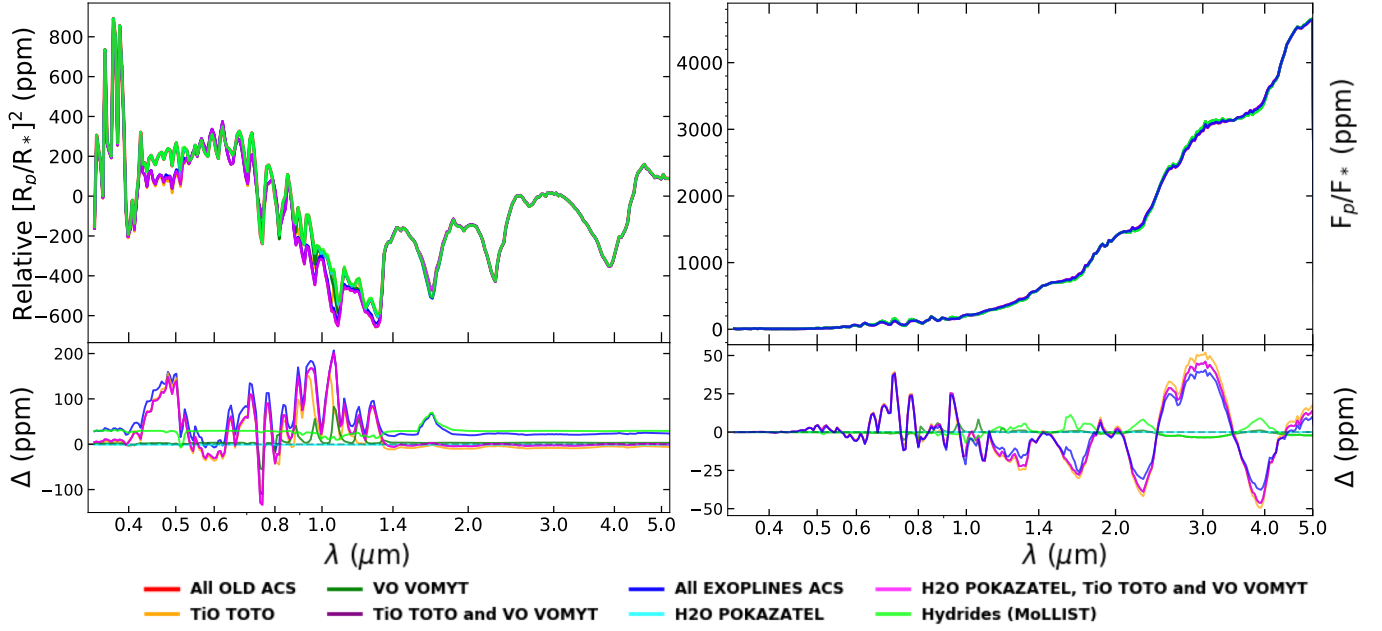


Figure 14. Impact of pre-generated opacities in the transmission and emission spectrum of a representative Ultra-Hot Jupiter. Transmission (Left) and Emission (Right) spectra calculated using opacities from all old ACSs (red) compared to all EXOPLINES ACSs (blue). Choice of linelists for TiO (TOTO vs Schwenke, in orange), VO (Plez vs VOMYT, in green), H₂O (Schwenke vs POKAZATEL, in cyan), and metal hydrides (in lime, see Table 7 references) along with combination differences of metal oxides (TiO and VO, in purple) as well as H₂O (magenta) showing notable residuals relative to all old ACS data (red) of up to 300 ppm, primarily in the optical bandpass, between 0.3-1.0 μm at *JWST* fiducial resolution at $R=100$ for transmission (Bottom Left) and up to 80 ppm in the infrared between 1.0-5.0 μm for thermal emission (Bottom Right), despite no significant shape differences amongst the spectra. In both cases, TiO produces the largest residual differences. Therefore, significant bias may arise with the choice of linelist in model atmospheres, especially when characterizing ultra hot Jupiter atmospheres with *JWST*.

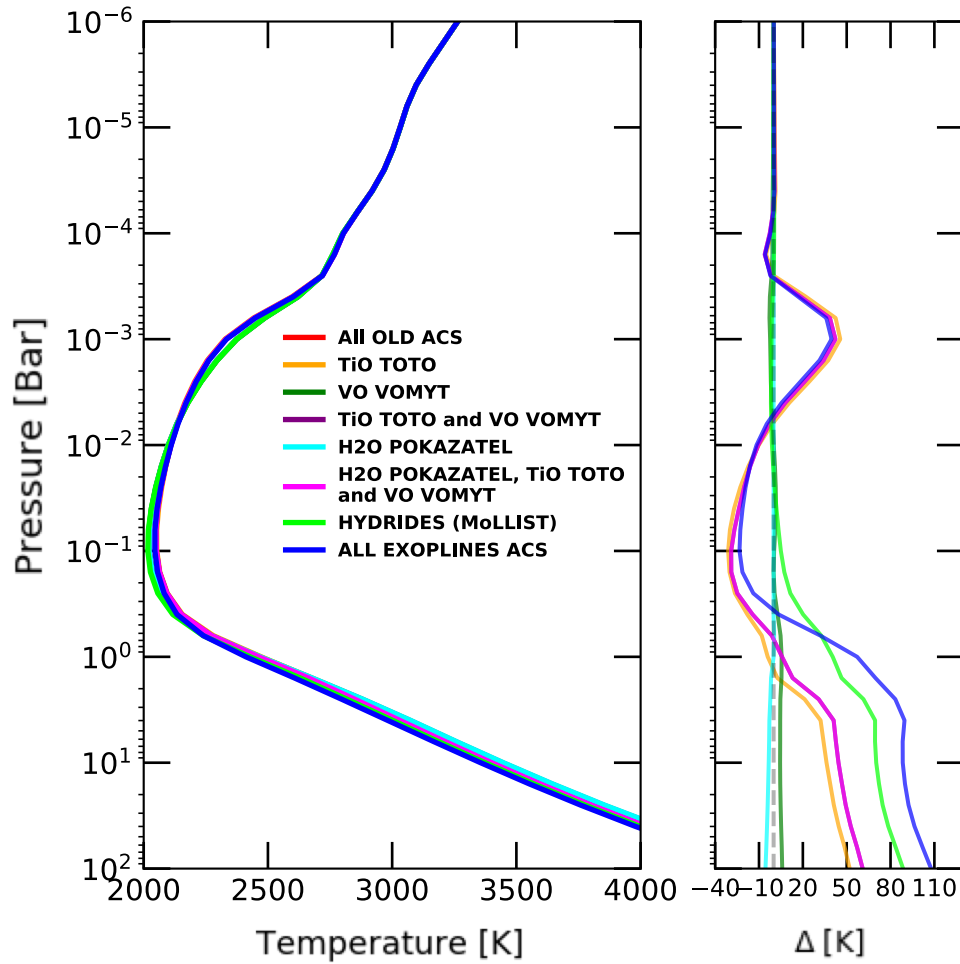


Figure 15. The impact of pre-generated opacities in the atmospheric structure of a representative Ultra-Hot Jupiter. (Left) Thermal structure calculated using pre-generated opacities from all old ACS (red) (Freedman et al. (2008), See Table 7), compared to EXOPLINES (blue). (Right) Independent effects of TiO (TOTO), VO (VOMYT), H₂O (POKAZATEL), metal hydrides (FeH/MgH/CaH/CrH-MoLLIST, and AlH-WYLLoT) (orange, green, cyan and lime respectively) as well as combination differences of all EXOPLINES ACS (blue) show variation in the thermal profile of up to 130 K for the same planet. The largest variations in the thermal profile are purely due to ACS differences of metal hydrides and oxides that are dominant in highly irradiated planet atmospheres.

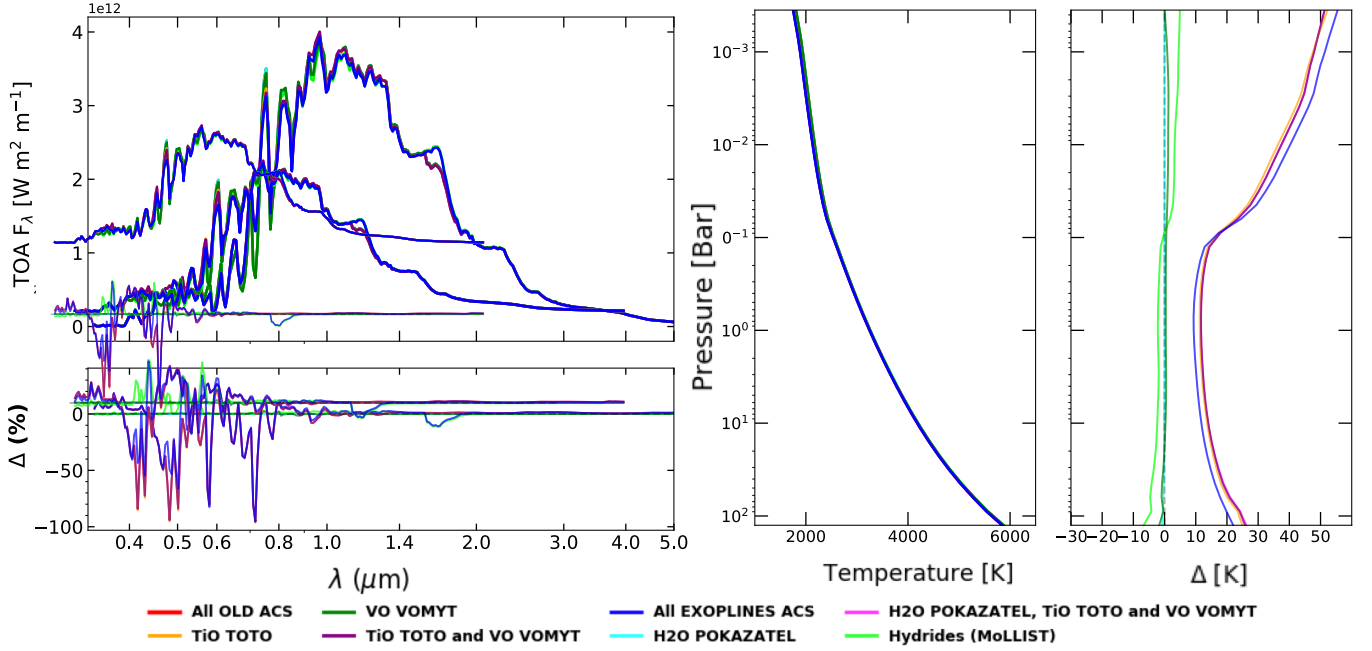


Figure 16. Impact of pre-generated opacities in characterizing a fiducial M-dwarf atmosphere, with T_{eff} of 3000 K, $\log(g)$ of 5 cm.s^{-2} , solar M/H, and C/O of 0.5. (Left) Model spectrum of the fiducial M-dwarf (showing top-of-atmosphere (TOA) flux) varying opacities calculated from all old ACS (red) compared to all EXOPLINES ACS (blue). Spectrum ($R=100$, covering $0.3\text{-}5\mu\text{m}$) calculated with TiO TOTO linelist (orange) attributes to largest residual differences in the spectral shape, with up to 125% in the optical bandpass below $1\mu\text{m}$, followed by 30% in residual differences caused purely due to the effect of metal hydride opacities (MoLLIST, lime) below $1\mu\text{m}$, and up to 12% between $1.4\text{-}2.0\mu\text{m}$. H_2O (POKAZATEL, cyan) and VO (VOMYT, green) alone do not induce noteworthy differences within the spectra. (Right) Atmospheric structure of fiducial M-dwarf, with respective residuals in the thermal profile. Consistent with the spectral differences, TiO linelist contributes to significant deviations within the T-P profile with up to 50 K above 0.1 bar in pressure, and up to 20 K down to 100 bars. The effect of both metal oxides (TiO and VO, purple), combined with H_2O (magenta) and along with all new opacities (EXOPLINES, blue) cause deviations in atmospheric structure of up to a maximum of 60 K.

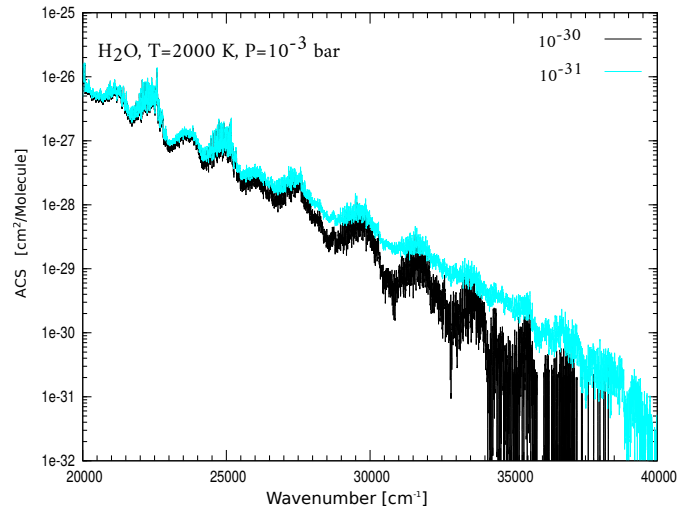


Figure 17. The impact of intensity cut-off on generating the H₂O *POKAZATEL* ACS data. Following Maxwell-Boltzmann distribution, the population of energy levels with high J quantum number increases with temperature. As a result, weak lines become stronger at high temperatures, and so insufficient intensity cut-off value results in accurate ACS. For instance, the choice of 10^{-30} (black) for intensity cut-off eliminate more lines in generating ACS data comparing to 10^{-31} $\text{cm}^{-1}/(\text{molecule cm}^{-2})$ (cyan). The reported cut-off values refer to 296 K.

REFERENCES

- Akpinar, S., & Akbalik, F. 2010, *Journal of Molecular Structure: THEOCHEM*, 942, 98 ,
doi: <https://doi.org/10.1016/j.theochem.2009.12.002>
- Alavi, S. F., & Shayesteh, A. 2017a, *MNRAS*, 474, 2,
doi: [10.1093/mnras/stx2681](https://doi.org/10.1093/mnras/stx2681)
- . 2017b, *MNRAS*, 474, 2, doi: [10.1093/mnras/stx2681](https://doi.org/10.1093/mnras/stx2681)
- Alberti, M., Weber, R., Mancini, M., Fateev, A., & Clausen, S. 2015, *JQSRT*, 157, 14 ,
doi: <https://doi.org/10.1016/j.jqsrt.2015.01.016>
- Allard, F., Hauschildt, P. H., & Schwenke, D. 2000, *ApJ*, 540, 1005, doi: [10.1086/309366](https://doi.org/10.1086/309366)
- Allard, N. F., Spiegelman, F., & Kielkopf, J. F. 2016, *A&A*, 589, A21, doi: [10.1051/0004-6361/201628270](https://doi.org/10.1051/0004-6361/201628270)
- Allard, N. F., Spiegelman, F., Leininger, T., & Molliere, P. 2019, *A&A*, 628, A120,
doi: [10.1051/0004-6361/201935593](https://doi.org/10.1051/0004-6361/201935593)
- Amiot, C., Azaroual, E. M., Luc, P., & Vetter, R. 1995, *JChPh*, 102, 4375, doi: [10.1063/1.469486](https://doi.org/10.1063/1.469486)
- Amundsen, D. S., Mayne, N. J., Baraffe, I., et al. 2016, *A & A*, 595, A36
- Anderson, P. W. 1949, *Physical Review*, 76, 647
- Andersson, N., Balfour, W. J., Bernath, P. F., Lindgren, B., & Ram, R. S. 2003, *JChPh*, 118, 3543,
doi: [10.1063/1.1539848](https://doi.org/10.1063/1.1539848)
- Arcangeli, J., Désert, J.-M., Line, M. R., et al. 2018, *ApJ*, 855, L30
- Babrov, H., Ameer, G., & Benesch, W. 1960, *The Journal of Chemical Physics*, 33, 145
- Balfour, W. J., Brown, J. M., & Wallace, L. 2004, *JChPh*, 121, 7735, doi: [10.1063/1.1797731](https://doi.org/10.1063/1.1797731)
- Balfour, W. J., & Cartwright, H. M. 1975a, *Canadian Journal of Physics*, 53, 1477, doi: [10.1139/p75-188](https://doi.org/10.1139/p75-188)
- . 1975b, *Chemical Physics Letters*, 32, 82,
doi: [10.1016/0009-2614\(75\)85173-6](https://doi.org/10.1016/0009-2614(75)85173-6)
- Balfour, W. J., Merer, A. J., Niki, H., Simard, B., & Hackett, P. A. 1993, *JChPh*, 99, 3288,
doi: [10.1063/1.465138](https://doi.org/10.1063/1.465138)
- Baranger, M. 1958, *Physical Review*, 111, 481,
doi: [10.1103/PhysRev.111.481](https://doi.org/10.1103/PhysRev.111.481)
- Barber, R. J., Tennyson, J., Harris, G. J., & Tolchenov, R. N. 2006, *MNRAS*, 368, 1087.
<https://arxiv.org/abs/0601236>
- Barklem, P. S., & Collet, R. 2016, *A&A*, 588, A96,
doi: [10.1051/0004-6361/201526961](https://doi.org/10.1051/0004-6361/201526961)
- Barrow, R., & Stone, T. 1975, *Journal of Physics B: Atomic and Molecular Physics*, 8, L13
- Barton, E. J., Hill, C., Yurchenko, S. N., et al. 2017, *JQSRT*, 187, 453. <https://arxiv.org/abs/1610.09008>
- Barton, E. J., Yurchenko, S. N., & Tennyson, J. 2013, *MNRAS*, 434, 1469, doi: [10.1093/mnras/stt1105](https://doi.org/10.1093/mnras/stt1105)
- Batalha, N., & Rooney, C. 2020,
doi: [10.5281/zenodo.4206648](https://doi.org/10.5281/zenodo.4206648)
- Batalha, N. E., Marley, M. S., Lewis, N. K., & Fortney, J. J. 2019, *ApJ*, 878, 70, doi: [10.3847/1538-4357/ab1b51](https://doi.org/10.3847/1538-4357/ab1b51)
- Batalha, N. M. 2014, *Proceedings of the National Academy of Sciences*, 111, 12647, doi: [10.1073/pnas.1304196111](https://doi.org/10.1073/pnas.1304196111)
- Bauschlicher, C. W., Ram, R. S., Bernath, P. F., Parsons, C. G., & Galehouse, D. 2001, *JChPh*, 115, 1312,
doi: [10.1063/1.1377892](https://doi.org/10.1063/1.1377892)
- Bean, J. L., Stevenson, K. B., Batalha, N. M., et al. 2018, *PASP*, 130, 114402, doi: [10.1088/1538-3873/aadbf3](https://doi.org/10.1088/1538-3873/aadbf3)
- Bernath, P. 2005, *Spectra of Atoms and Molecules*, 2nd edn. (Oxford University Press)
- . 2020a, *ApJ*, 895, 87, doi: [10.3847/1538-4357/ab7cd0](https://doi.org/10.3847/1538-4357/ab7cd0)
- Bernath, P. F. 2020b, *JQSRT*, 240, 106687,
doi: <https://doi.org/10.1016/j.jqsrt.2019.106687>
- Bézar, B., Fedorova, A., Bertaux, J.-L., Rodin, A., & Korablev, O. 2011, *Icarus*, 216, 173
- Birkby, J. L., de Kok, R. J., Brogi, M., et al. 2013, *MNRAS*, 436, L35, doi: [10.1093/mnrasl/slt107](https://doi.org/10.1093/mnrasl/slt107)
- Bittner, D. M., & Bernath, P. F. 2018, *ApJS*, 236, 46,
doi: [10.3847/1538-4365/aabfe8](https://doi.org/10.3847/1538-4365/aabfe8)
- Brandes, G. R., & Galehouse, D. C. 1985, *JMS*, 109, 345,
doi: [10.1016/0022-2852\(85\)90317-0](https://doi.org/10.1016/0022-2852(85)90317-0)
- Brogi, M., & Line, M. R. 2019, *AJ*, 157, 114
- Buldyreva, J., Lavrentieva, N., & Starikov, V. 2011, *Collisional Line Broadening and Shifting of Atmospheric Gases* (World Scientific Publishing Co)
- Burrows, A., Dulick, M., Bauschlicher, C. W., J., et al. 2005, *ApJ*, 624, 988, doi: [10.1086/429366](https://doi.org/10.1086/429366)
- Burrows, A., Dulick, M., C. W. Bauschlicher, J., et al. 2005, *ApJ*, 624, 988, doi: [10.1086/429366](https://doi.org/10.1086/429366)
- Burrows, A., Ram, R. S., Bernath, P., Sharp, C. M., & Milsom, J. A. 2002, *ApJ*, 577, 986, doi: [10.1086/342242](https://doi.org/10.1086/342242)
- Burrows, A., & Sharp, C. 1999, *ApJ*, 512, 843
- Campbell, J. M., Klapstein, D., Dulick, M., Bernath, P. F., & Wallace, L. 1995, *ApJS*, 101, 237, doi: [10.1086/192238](https://doi.org/10.1086/192238)
- Cappelletti, D., Bartolomei, M., Sabido, M., et al. 2005, *The Journal of Physical Chemistry A*, 109, 8471
- Cheung, A.-C., Taylor, A., & Merer, A. 1982, *JMS*, 92, 391 , doi: [https://doi.org/10.1016/0022-2852\(82\)90110-2](https://doi.org/10.1016/0022-2852(82)90110-2)
- Chubb, K. L., Rocchetto, M., Yurchenko, S. N., et al. 2020, *arXiv e-prints*, arXiv:2009.00687.
<https://arxiv.org/abs/2009.00687>
- Conway, E. K., Gordon, I. E., Tennyson, J., et al. 2020, *Atmospheric Chemistry and Physics*, 20, 10015,
doi: [10.5194/acp-20-10015-2020](https://doi.org/10.5194/acp-20-10015-2020)

- Cushing, M. C., Rayner, J. T., Davis, S. P., & Vacca, W. D. 2003, *ApJ*, 582, 1066, doi: [10.1086/344525](https://doi.org/10.1086/344525)
- Cushing, M. C., Rayner, J. T., & Vacca, W. D. 2005, *ApJ*, 623, 1115, doi: [10.1086/428040](https://doi.org/10.1086/428040)
- Dayou, F., & Balança, C. 2006, *A&A*, 459, 297, doi: [10.1051/0004-6361:20065718](https://doi.org/10.1051/0004-6361:20065718)
- Delfosse, X., Tinney, C. G., Forveille, T., et al. 1997, *A&A*, 327, L25
- Devi, M. V., Chris Benner, D., Smith, M., et al. 2012, *Journal of Quantitative Spectroscopy and Radiative Transfer*, 113, 1013, doi: <https://doi.org/10.1016/j.jqsrt.2012.02.010>
- Devi, M. V., Predoi-Cross, A., Chris Benner, D., et al. 2004, *Journal of Molecular Spectroscopy*, 228, 580, doi: <https://doi.org/10.1016/j.jms.2004.05.006>
- Dulick, M., C. W. Bauschlicher, J., Burrows, A., et al. 2003, *ApJ*, 594, 651, doi: [10.1086/376791](https://doi.org/10.1086/376791)
- Fortney, J. J., Lodders, K., Marley, M. S., & Freedman, R. S. 2008, *ApJ*, 678, 1419, doi: [10.1086/528370](https://doi.org/10.1086/528370)
- Fortney, J. J., Mordasini, C., Nettelmann, N., et al. 2013, *ApJ*, 775, 80. <https://arxiv.org/abs/1306.4329>
- Fortney, J. J., Robinson, T. D., Domagal-Goldman, S., et al. 2019, arXiv e-prints. <https://arxiv.org/abs/1905.07064>
- Freedman, R. S., Lustig-Yaeger, J., Fortney, J. J., et al. 2014, *ApJS*, 214. <https://arxiv.org/abs/1409.0026>
- Freedman, R. S., Marley, M. S., & Lodders, K. 2008, *ApJS*, 174, 504. <https://arxiv.org/abs/0706.2374>
- Gamache, R. R., & Vispoel, B. 2018, *Journal of Quantitative Spectroscopy and Radiative Transfer*, 217, 440
- Gandhi, S., & Madhusudhan, N. 2019, *MNRAS*, 485, 5817, doi: [10.1093/mnras/stz751](https://doi.org/10.1093/mnras/stz751)
- Gandhi, S., Brogi, M., Yurchenko, S. N., et al. 2020, *MNRAS*, doi: [10.1093/mnras/staa981](https://doi.org/10.1093/mnras/staa981)
- Gharib-Nezhad, E., Heays, A. N., Bechtel, H. A., & Lyons, J. R. 2019, *JQSRT*, 239, 106649, doi: <https://doi.org/10.1016/j.jqsrt.2019.106649>
- Gharib-Nezhad, E., & Line, M. R. 2019, *ApJ*, 872, 27
- GharibNezhad, E., Shayesteh, A., & Bernath, P. F. 2013, *MNRAS*, 432, 2043, doi: [10.1093/mnras/stt510](https://doi.org/10.1093/mnras/stt510)
- Gierszal, S., Galica, J., & Miś-Kuźmińska, E. 1998, *The Journal of Chemical Physics*, 108, 8976, doi: [10.1063/1.476343](https://doi.org/10.1063/1.476343)
- Gordon, I. E., Rothman, L. S., Hill, C., et al. 2017, *JQSRT*, 203, 3, doi: [10.1016/j.jqsrt.2017.06.038](https://doi.org/10.1016/j.jqsrt.2017.06.038)
- Goyal, J. M., Mayne, N., Sing, D. K., et al. 2018, *MNRAS*, 474, 5158, doi: [10.1093/mnras/stx3015](https://doi.org/10.1093/mnras/stx3015)
- Greene, T. P., Line, M. R., Montero, C., et al. 2016, *ApJ*, 817, 17, doi: [10.3847/0004-637X/817/1/17](https://doi.org/10.3847/0004-637X/817/1/17)
- Grigoriev, I., Doucen, R. L., Boissoles, J., et al. 1999, *JMS*, 198, 249, doi: <https://doi.org/10.1006/jmsp.1999.7903>
- Grimm, S. L., Malik, M., Kitzmann, D., et al. 2021, *ApJS*, 253, 30, doi: [10.3847/1538-4365/abd773](https://doi.org/10.3847/1538-4365/abd773)
- Hargreaves, R. J., Hinkle, K. H., Bauschlicher, C. W., et al. 2010, *AJ*, 140, 919, doi: [10.1088/0004-6256/140/4/919](https://doi.org/10.1088/0004-6256/140/4/919)
- Hartmann, J. M., Boulet, C., Brodbeck, C., et al. 2002, *JQSRT*, 72, 117, doi: [10.1016/S0022-4073\(01\)00058-9](https://doi.org/10.1016/S0022-4073(01)00058-9)
- Hartmann, J.-M., Boulet, C., & Robert, D. 2021, *Collisional effects on molecular spectra: laboratory experiments and models, consequences for applications* (Elsevier)
- Hartmann, J.-M., Tran, H., Armante, R., et al. 2018, *JQSRT*, 213, 178, doi: [10.1016/j.jqsrt.2018.03.016](https://doi.org/10.1016/j.jqsrt.2018.03.016)
- Herman, M. K., de Mooij, E. J. W., Jayawardhana, R., & Brogi, M. 2020, arXiv e-prints, arXiv:2006.10743. <https://arxiv.org/abs/2006.10743>
- Hodges, J. N., & Bernath, P. F. 2018, *ApJ*, 863, 36, doi: [10.3847/1538-4357/aacf07](https://doi.org/10.3847/1538-4357/aacf07)
- Hoeijmakers, H. J., de Kok, R. J., Snellen, I. A. G., et al. 2015, *A&A*, 575, A20, doi: [10.1051/0004-6361/201424794](https://doi.org/10.1051/0004-6361/201424794)
- Hopkins, W. S., Hamilton, S. M., & Mackenzie, S. R. 2009, *The Journal of Chemical Physics*, 130, 144308, doi: [10.1063/1.3104844](https://doi.org/10.1063/1.3104844)
- Hörst, S. M., He, C., Lewis, N. K., et al. 2018, *Nature Astronomy*, 2, 303, doi: [10.1038/s41550-018-0397-0](https://doi.org/10.1038/s41550-018-0397-0)
- Huang, G., Merer, A. J., & Clouthier, D. J. 1992, *JMS*, 153, 32, doi: [https://doi.org/10.1016/0022-2852\(92\)90455-W](https://doi.org/10.1016/0022-2852(92)90455-W)
- Hubeny, I., Burrows, A., & Sudarsky, D. 2003, *ApJ*, 594, 1011, doi: [10.1086/377080](https://doi.org/10.1086/377080)
- Hübner, O., Hornung, J., & Himmel, H.-J. 2015, *JChPh*, 143, 024309, doi: [10.1063/1.4926393](https://doi.org/10.1063/1.4926393)
- Humlíček, J. 1979, *JQSRT*, 21, 309
- Iyer, A. R., Line, M. R., & Gharib-Nezhad, E. In *Prep Kataria, T., Sing, D. K., Lewis, N. K., et al. 2016, ApJ*, 821, 9
- Kempton, E. M.-R., Lupu, R., Owusu-Asare, A., Slough, P., & Cale, B. 2017, *PASP*, 129, 044402, doi: [10.1088/1538-3873/aa61ef](https://doi.org/10.1088/1538-3873/aa61ef)
- Kempton, E. M. R., Bean, J. L., Louie, D. R., et al. 2018, *PASP*, 130, 114401, doi: [10.1088/1538-3873/aadf6f](https://doi.org/10.1088/1538-3873/aadf6f)
- Kirkpatrick, J. D. 2005, *ARA&A*, 43, 195
- Kirkpatrick, J. D., Barman, T. S., Burgasser, A. J., et al. 2006, *ApJ*, 639, 1120, doi: [10.1086/499622](https://doi.org/10.1086/499622)
- Kirkpatrick, J. D., Henry, T. J., & McCarthy, Donald W., J. 1991, *ApJS*, 77, 417, doi: [10.1086/191611](https://doi.org/10.1086/191611)
- Kirkpatrick, J. D., Reid, I. N., Liebert, J., et al. 1999, *ApJ*, 519, 802, doi: [10.1086/307414](https://doi.org/10.1086/307414)
- . 2000, *AJ*, 120, 447, doi: [10.1086/301427](https://doi.org/10.1086/301427)
- Kochanov, R. V., Gordon, I. E., Rothman, L. S., et al. 2016, *JQSRT*, 177, 15, doi: [10.1016/j.jqsrt.2016.03.005](https://doi.org/10.1016/j.jqsrt.2016.03.005)

- Kreidberg, L., Bean, J. L., Désert, J. M., et al. 2014, *ApJL*, 793, 2. <https://arxiv.org/abs/1410.2255>
- Kurucz, R. L. 1992, *RMxAA*, 23, 45
- Langhoff, S. R. 1997, *ApJ*, 481, 1007, doi: [10.1086/304077](https://doi.org/10.1086/304077)
- Langhoff, S. R., & Arnold, J. 1979, *The Journal of Chemical Physics*, 70, 852
- Langhoff, S. R., & Bauschlicher, C. W. 1993, *Chemical Physics Letters*, 211, 305 , doi: [https://doi.org/10.1016/0009-2614\(93\)87064-A](https://doi.org/10.1016/0009-2614(93)87064-A)
- Launila, O., & Lindgren, B. 1996, *JChPh*, 104, 6418, doi: [10.1063/1.471362](https://doi.org/10.1063/1.471362)
- Li, G., Asfin, R. E., Domanskaya, A. V., & Ebert, V. 2018, *Molecular Physics*, 116, 3495
- Li, G., Harrison, J. J., Ram, R. S., Western, C. M., & Bernath, P. F. 2012, *JQSRT*, 113, 67, doi: [10.1016/j.jqsrt.2011.09.010](https://doi.org/10.1016/j.jqsrt.2011.09.010)
- Li, G., Harrison, J. J., Ram, R. S., Western, C. M., & Bernath, P. F. 2012, *JQSRT*, 113, 67 , doi: <https://doi.org/10.1016/j.jqsrt.2011.09.010>
- Line, M. R., Knutson, H., Wolf, A. S., & Yung, Y. L. 2014, *ApJ*, 783, 70
- Line, M. R., Stevenson, K. B., Bean, J., et al. 2016, *AJ*, 152, 203
- Linton, C., Steimle, T. C., & Frey, S. E. 2012, *JMS*, 279, 1, doi: [10.1016/j.jms.2012.07.017](https://doi.org/10.1016/j.jms.2012.07.017)
- Lockwood, G. W. 1972, *ApJS*, 24, 375, doi: [10.1086/190259](https://doi.org/10.1086/190259)
- Lodders, K. 1999, *ApJ*, 519, 793, doi: [10.1086/307387](https://doi.org/10.1086/307387)
- Lodders, K., & Fegley, B., J. 2006, *Chemistry of Low Mass Substellar Objects*, ed. J. W. Mason, 1, doi: [10.1007/3-540-30313-8_1](https://doi.org/10.1007/3-540-30313-8_1)
- Louie, D. R., Deming, D., Albert, L., et al. 2018, *PASP*, 130, 044401. <https://arxiv.org/abs/1711.02098>
- Lupu, R. E., Zahnle, K., Marley, M. S., et al. 2014, *ApJ*, 784, 27, doi: [10.1088/0004-637X/784/1/27](https://doi.org/10.1088/0004-637X/784/1/27)
- Ma, Q., Tipping, R., & Boulet, C. 2007, *JQSRT*, 103, 588
- MacDonald, R. J. 2019, PhD thesis, University of Cambridge
- Madhusudhan, N. 2019, *ARA&A*, 57, 617, doi: [10.1146/annurev-astro-081817-051846](https://doi.org/10.1146/annurev-astro-081817-051846)
- Malik, M., Kitzmann, D., Mendonça, J. M., et al. 2019, *AJ*, 157, 170, doi: [10.3847/1538-3881/ab1084](https://doi.org/10.3847/1538-3881/ab1084)
- Mantz, A., Devi, V. M., Benner, D. C., et al. 2005, *Journal of molecular structure*, 742, 99
- Marley, M. S., & Robinson, T. D. 2015, *ARA&A*, 53, 279. <https://arxiv.org/abs/1410.6512>
- Matos, J. M. O., Malmqvist, P.-Å., & Roos, B. O. 1987, *JChPh*, 86, 5032, doi: [10.1063/1.452679](https://doi.org/10.1063/1.452679)
- McCormack, P., & Oconnor, S. 1976, *A&AS*, 26, 373
- McKemmish, L. K., Masseron, T., Hoeijmakers, H. J., et al. 2019a, *MNRAS*, 488, 2836, doi: [10.1093/mnras/stz1818](https://doi.org/10.1093/mnras/stz1818)
- . 2019b, *MNRAS*, 488, 2836, doi: [10.1093/mnras/stz1818](https://doi.org/10.1093/mnras/stz1818)
- McKemmish, L. K., Yurchenko, S. N., & Tennyson, J. 2016, *MNRAS*, 463, 771, doi: [10.1093/mnras/stw1969](https://doi.org/10.1093/mnras/stw1969)
- Melin, S. T., & Sanders, S. T. 2016, *JQSRT*, 180, 184 , doi: <https://doi.org/10.1016/j.jqsrt.2016.04.009>
- Merer, A., Huang, G., Cheung, A.-C., & Taylor, A. 1987, *JMS*, 125, 465 , doi: [https://doi.org/10.1016/0022-2852\(87\)90110-X](https://doi.org/10.1016/0022-2852(87)90110-X)
- Merritt, S. R., Gibson, N. P., Nugroho, S. K., et al. 2020, *A&A*, 636, A117, doi: [10.1051/0004-6361/201937409](https://doi.org/10.1051/0004-6361/201937409)
- Miliordos, E., & Mavridis, A. 2007, *The Journal of Physical Chemistry A*, 111, 1953, doi: [10.1021/jp067451b](https://doi.org/10.1021/jp067451b)
- Molaverdikhani, K., Henning, T., & Mollière, P. 2019, *ApJ*, 873, 32, doi: [10.3847/1538-4357/aafda8](https://doi.org/10.3847/1538-4357/aafda8)
- Mollière, P., Wardenier, J., van Boekel, R., et al. 2019, *Astronomy & Astrophysics*, 627, A67
- Mordasini, C., van Boekel, R., Mollière, P., Henning, T., & Benneke, B. 2016, *ApJ*, 832, 1. <https://arxiv.org/abs/1609.03019>
- Ngo, N., Lisak, D., Tran, H., & Hartmann, J.-M. 2013, *JQSRT*, 129, 89 , doi: <https://doi.org/10.1016/j.jqsrt.2013.05.034>
- Ngo, N. H., Tran, H., Gamache, R. R., & Hartmann, J. M. 2012, *Philosophical Transactions of the Royal Society of London Series A*, 370, 2495, doi: [10.1098/rsta.2011.0272](https://doi.org/10.1098/rsta.2011.0272)
- Nugroho, S. K., Gibson, N. P., de Mooij, E. J. W., et al. 2020, *MNRAS*, 496, 504, doi: [10.1093/mnras/staa1459](https://doi.org/10.1093/mnras/staa1459)
- Nugroho, S. K., Kawahara, H., Masuda, K., et al. 2017, *AJ*, 154, 221, doi: [10.3847/1538-3881/aa9433](https://doi.org/10.3847/1538-3881/aa9433)
- Öberg, K. I., Murray-Clay, R., & Bergin, E. A. 2011, *ApJL*, 743, L16. <https://arxiv.org/abs/1110.5567>
- Odashima, H., Kajita, M., Matsuo, Y., Minowa, T., & Shimizu, T. 1989, *The Journal of Chemical Physics*, 90, 4875, doi: [10.1063/1.456581](https://doi.org/10.1063/1.456581)
- Partridge, H., & Schwenke, D. W. 1997, *JCP*, 106, 4618
- Peterson, D. E., Megeath, S. T., Luhman, K. L., et al. 2008, *ApJ*, 685, 313, doi: [10.1086/590527](https://doi.org/10.1086/590527)
- Phillips, J. G., Davis, S. P., Lindgren, B., & Balfour, W. J. 1987a, *ApJS*, 65, 721, doi: [10.1086/191241](https://doi.org/10.1086/191241)
- . 1987b, *ApJS*, 65, 721, doi: [10.1086/191241](https://doi.org/10.1086/191241)
- Pickett, H. M. 1980, *The Journal of Chemical Physics*, 73, 6090, doi: [10.1063/1.440145](https://doi.org/10.1063/1.440145)
- Piette, A. A. A., Madhusudhan, N., McKemmish, L. K., et al. 2020, arXiv e-prints, arXiv:2006.04807. <https://arxiv.org/abs/2006.04807>
- Piskorz, D., Buzard, C., Line, M. R., et al. 2018, *AJ*, 156, 133, doi: [10.3847/1538-3881/aad781](https://doi.org/10.3847/1538-3881/aad781)
- Plez, B. 1998, *A&A*, 337, 495
- Plez, B. 1999, in *Asymptotic Giant Branch Stars*, ed. T. Le Bertre, A. Lebre, & C. Waelkens, Vol. 191, 75

- Plez, B., Brett, J. M., & Nordlund, A. 1992, *A&A*, 256, 551
- Polyansky, O. L., Kyuberis, A. A., Zobov, N. F., et al. 2018, *MNRAS*, 480, 2597, doi: [10.1093/mnras/sty1877](https://doi.org/10.1093/mnras/sty1877)
- Polyansky, O. L., Zobov, N. F., Mizus, I. I., et al. 2018, *JQSRT*, 210, 127
- Ram, R., Bernath, P., Davis, S., & Merer, A. 2002, *JMS*, 211, 279, doi: <https://doi.org/10.1006/jmsp.2001.8510>
- Ram, R., Bernath, P., & Wallace, L. 1996, *ApJ Supplement Series*, 107, 443
- Ram, R. S., & Bernath, P. F. 1996, *ApOpt*, 35, 2879, doi: [10.1364/AO.35.002879](https://doi.org/10.1364/AO.35.002879)
- 2005, *JMS*, 229, 57, doi: [10.1016/j.jms.2004.08.014](https://doi.org/10.1016/j.jms.2004.08.014)
- Ram, R. S., Bernath, P. F., Dulick, M., & Wallace, L. 1999, *ApJS*, 122, 331, doi: [10.1086/313212](https://doi.org/10.1086/313212)
- Ram, R. S., Jarman, C. N., & Bernath, P. F. 1993, *JMS*, 161, 445, doi: [10.1006/jmsp.1993.1250](https://doi.org/10.1006/jmsp.1993.1250)
- Ram, R. S., Tereszchuk, K., Gordon, I. E., Walker, K. A., & Bernath, P. F. 2011, *JMS*, 266, 86, doi: [10.1016/j.jms.2011.03.009](https://doi.org/10.1016/j.jms.2011.03.009)
- Reid, I. N., Burgasser, A. J., Cruz, K. L., Kirkpatrick, J. D., & Gizis, J. E. 2001, *AJ*, 121, 1710, doi: [10.1086/319418](https://doi.org/10.1086/319418)
- Reid, I. N., & Hawley, S. L. 2005, *New light on dark stars : red dwarfs, low-mass stars, brown dwarfs* (Praxis Publishing Ltd), doi: [10.1007/3-540-27610-6](https://doi.org/10.1007/3-540-27610-6)
- Renaud, C. L., Cleghorn, K., Hartmann, L., Vispoel, B., & Gamache, R. R. 2018, *Icarus*, 306, 275, doi: [10.1016/j.icarus.2017.10.016](https://doi.org/10.1016/j.icarus.2017.10.016)
- Robert, D., & Bonamy, J. 1979, *Journal de Physique*, 40, 923
- Rothman, L., Gordon, I., Barber, R., et al. 2010, *JQSRT*, 111, 2139
- Rothman, L. S., Jacquemart, D., Barbe, A., et al. 2005, *Journal of quantitative spectroscopy and radiative transfer*, 96, 139
- Ruiz, M. T., Leggett, S. K., & Allard, F. 1997, *ApJL*, 491, L107, doi: [10.1086/311070](https://doi.org/10.1086/311070)
- Régalia-Jarlot, L., Thomas, X., Von der Heyden, P., & Barbe, A. 2005, *Journal of Quantitative Spectroscopy and Radiative Transfer*, 91, 121, doi: <https://doi.org/10.1016/j.jqsrt.2004.05.042>
- Schiavon, R. P., Barbuy, B., & Singh, P. D. 1997, *ApJ*, 484, 499, doi: [10.1086/304332](https://doi.org/10.1086/304332)
- Schreier, F. 2018a, *MNRAS*, 479, 3068, doi: [10.1093/mnras/sty1680](https://doi.org/10.1093/mnras/sty1680)
- 2018b, *JQSRT*, 213, 13, doi: [10.1016/j.jqsrt.2018.03.019](https://doi.org/10.1016/j.jqsrt.2018.03.019)
- Schwenke, D. W. 1998, *Faraday Discussions*, 109, 321
- Schwenke, D. W. 1998, *Faraday Discussions*, 109, 321, doi: [10.1039/a800070k](https://doi.org/10.1039/a800070k)
- Sharp, C. M., & Burrows, A. 2007, *ApJS*, 168, 140, <https://arxiv.org/abs/0607211>
- Sharpless, S. 1956, *ApJ*, 124, 342, doi: [10.1086/146229](https://doi.org/10.1086/146229)
- Shayesteh, A., Alavi, S. F., Rahman, M., & Gharib-Nezhad, E. 2017, *Chemical Physics Letters*, 667, 345, doi: [10.1016/j.cplett.2016.11.020](https://doi.org/10.1016/j.cplett.2016.11.020)
- Shayesteh, A., & Bernath, P. F. 2011, *JChPh*, 135, 094308, doi: [10.1063/1.3631341](https://doi.org/10.1063/1.3631341)
- Shayesteh, A., Ram, R. S., & Bernath, P. F. 2013, *JMS*, 288, 46, doi: [10.1016/j.jms.2013.04.009](https://doi.org/10.1016/j.jms.2013.04.009)
- Shayesteh, A., Walker, K. A., Gordon, I., Appadoo, D. R. T., & Bernath, P. F. 2004, *Journal of Molecular Structure*, 695-696, 23, doi: [10.1016/j.molstruc.2003.11.001](https://doi.org/10.1016/j.molstruc.2003.11.001)
- Sonnabend, G., Wirtz, D., Schieder, R., & Bernath, P. F. 2006, *Solar Physics*, 233, 205, doi: [10.1007/s11207-006-2488-9](https://doi.org/10.1007/s11207-006-2488-9)
- Sousa-Silva, C., Hesketh, N., Yurchenko, S. N., Hill, C., & Tennyson, J. 2014, *JQSRT*, 142, 66, doi: [10.1016/j.jqsrt.2014.03.012](https://doi.org/10.1016/j.jqsrt.2014.03.012)
- Steimle, T. C., Shirley, J. E., Simard, B., Vasseur, M., & Hackett, P. 1991, *JChPh*, 95, 7179, doi: [10.1063/1.461394](https://doi.org/10.1063/1.461394)
- Steimle, T. C., & Virgo, W. 2003, *Chemical Physics Letters*, 381, 30, doi: [10.1016/j.cplett.2003.09.102](https://doi.org/10.1016/j.cplett.2003.09.102)
- Sullivan, P. W., Winn, J. N., Berta-Thompson, Z. K., et al. 2015, *ApJ*, 809, 77, <https://arxiv.org/abs/1506.03845>
- Szajna, W., & Zachwieja, M. 2009, *European Physical Journal D*, 55, 549, doi: [10.1140/epjd/e2009-00253-y](https://doi.org/10.1140/epjd/e2009-00253-y)
- 2010, *JMS*, 260, 130, doi: [10.1016/j.jms.2010.02.004](https://doi.org/10.1016/j.jms.2010.02.004)
- Tan, Y., Kochanov, R. V., Rothman, L. S., & Gordon, I. E. 2019, *Journal of Geophysical Research: Atmospheres*, 124, 11580, doi: [10.1029/2019JD030929](https://doi.org/10.1029/2019JD030929)
- Tennyson, J., Yurchenko, S. N., Al-Refaie, A. F., et al. 2020, *JQSRT*, 255, 107228, doi: [10.1016/j.jqsrt.2020.107228](https://doi.org/10.1016/j.jqsrt.2020.107228)
- Tinney, C. G., & Reid, I. N. 1998, *MNRAS*, 301, 1031, doi: [10.1046/j.1365-8711.1998.02079.x](https://doi.org/10.1046/j.1365-8711.1998.02079.x)
- Toth, R. A., Hunt, R. H., & Plyler, E. K. 1970, *JChPh*, 53, 4303, doi: [10.1063/1.1673937](https://doi.org/10.1063/1.1673937)
- van den Bekerom, D. C. M., & Pannier, E. 2021, *JQSRT*, 261, 107476, doi: [10.1016/j.jqsrt.2020.107476](https://doi.org/10.1016/j.jqsrt.2020.107476)
- Veillard, A. 2012, *Quantum chemistry: the challenge of transition metals and coordination chemistry*, Vol. 176 (Springer Science & Business Media)
- Vidler, M., & Tennyson, J. 2000, *JChPh*, 113, 9766, doi: [10.1063/1.1321769](https://doi.org/10.1063/1.1321769)
- Villanueva, G., Smith, M., Protopapa, S., Faggi, S., & Mandell, A. 2018, *JQSRT*, 217, 86, doi: <https://doi.org/10.1016/j.jqsrt.2018.05.023>
- Vispoel, B., Cavalcanti, J. H., Paige, E. T., & Gamache, R. R. 2020, *JQSRT*, 253, 107030, doi: <https://doi.org/10.1016/j.jqsrt.2020.107030>

- Visscher, C., Lodders, K., & Fegley, Bruce, J. 2010, *ApJ*, 716, 1060, doi: [10.1088/0004-637X/716/2/1060](https://doi.org/10.1088/0004-637X/716/2/1060)
- Wagner, G., Birk, M., Gamache, R. R., & Hartmann, J. M. 2005, *JQSRT*, 92, 211, doi: [10.1016/j.jqsrt.2004.07.023](https://doi.org/10.1016/j.jqsrt.2004.07.023)
- Watson, W. W., & Hull, G. F. 1936, *Physical Review*, 49, 592, doi: [10.1103/PhysRev.49.592](https://doi.org/10.1103/PhysRev.49.592)
- Webber, J. C. 1971, *SoPh*, 16, 340, doi: [10.1007/BF00162476](https://doi.org/10.1007/BF00162476)
- Weck, P. F., Stancil, P. C., & Kirby, K. 2003, *JChPh*, 118, 9997, doi: [10.1063/1.1573181](https://doi.org/10.1063/1.1573181)
- Wende, S., Reiners, A., Seifahrt, A., & Bernath, P. F. 2010, *A&A*, 523, A58, doi: [10.1051/0004-6361/201015220](https://doi.org/10.1051/0004-6361/201015220)
- Yadin, B., Veness, T., Conti, P., et al. 2012, *MNRAS*, 425, 34, doi: [10.1111/j.1365-2966.2012.21367.x](https://doi.org/10.1111/j.1365-2966.2012.21367.x)
- Yang, B., Zhang, P., Qu, C., et al. 2018, *The Journal of Physical Chemistry A*, 122, 1511
- Yurchenko, S. N., Al-Refaie, A. F., & Tennyson, J. 2018, *A&A*, 614, A131, doi: [10.1051/0004-6361/201732531](https://doi.org/10.1051/0004-6361/201732531)
- Yurchenko, S. N., Williams, H., Leyland, P. C., Lodi, L., & Tennyson, J. 2018, *MNRAS*, 479, 1401, doi: [10.1093/mnras/sty1524](https://doi.org/10.1093/mnras/sty1524)
- Zaghloul, M. R. 2015, arXiv preprint arXiv:1505.05596
- Zhang, X. 2020, *Research in Astronomy and Astrophysics*, 20, 099, doi: [10.1088/1674-4527/20/7/99](https://doi.org/10.1088/1674-4527/20/7/99)